

Chemical Science

Accepted Manuscript



This is an *Accepted Manuscript*, which has been through the Royal Society of Chemistry peer review process and has been accepted for publication.

Accepted Manuscripts are published online shortly after acceptance, before technical editing, formatting and proof reading. Using this free service, authors can make their results available to the community, in citable form, before we publish the edited article. We will replace this *Accepted Manuscript* with the edited and formatted *Advance Article* as soon as it is available.

You can find more information about *Accepted Manuscripts* in the [Information for Authors](#).

Please note that technical editing may introduce minor changes to the text and/or graphics, which may alter content. The journal's standard [Terms & Conditions](#) and the [Ethical guidelines](#) still apply. In no event shall the Royal Society of Chemistry be held responsible for any errors or omissions in this *Accepted Manuscript* or any consequences arising from the use of any information it contains.

ARTICLE

Metal oxidation states in biological water splitting

Cite this: DOI: 10.1039/x0xx00000x

Vera Krewald^a, Marius Retegan^a, Nicholas Cox^a, Johannes Messinger^b, Wolfgang Lubitz^a, Serena DeBeer^a, Frank Neese^a, Dimitrios A. Pantazis^{a*}Received 00th January 2012,
Accepted 00th January 2012

DOI: 10.1039/x0xx00000x

www.rsc.org/

A central question in biological water splitting concerns the oxidation states of the manganese ions that comprise the oxygen-evolving complex of photosystem II. Understanding the nature and order of oxidation events that occur during the catalytic cycle of five S_i states ($i = 0-4$) is of fundamental importance both for the natural system and for artificial water oxidation catalysts. Despite the widespread adoption of the so-called "high-valent scheme"—where, for example, the Mn oxidation states in the S_2 state are assigned as III, IV, IV, IV—the competing "low-valent scheme" that differs by a total of two metal unpaired electrons (i.e. III, III, III, IV in the S_2 state) is favored by several recent studies for the biological catalyst. The question of the correct oxidation state assignment is addressed here by a detailed computational comparison of the two schemes using a common structural platform and theoretical approach. Models based on crystallographic constraints were constructed for all conceivable oxidation state assignments in the four (semi)stable S states of the oxygen evolving complex, sampling various protonation levels and patterns to ensure comprehensive coverage. The models are evaluated with respect to their geometric, energetic, electronic, and spectroscopic properties against available experimental EXAFS, XFEL-XRD, EPR, ENDOR and Mn K pre-edge XANES data. New 2.5 K ^{55}Mn ENDOR data of the S_2 state are also reported. Our results conclusively show that the entire S state phenomenology can only be accommodated within the high-valent scheme by adopting a single motif and protonation pattern that progresses smoothly from S_0 (III, III, III, IV) to S_3 (IV, IV, IV, IV), satisfying all experimental constraints and reproducing all observables. By contrast, it was impossible to construct a consistent cycle based on the low-valent scheme for all S states. Instead, the low-valent models developed here may provide new insight into the over-reduced S states and the states involved in the assembly of the catalytically active water oxidizing cluster.

INTRODUCTION

Large-scale water splitting using earth-abundant transition metal catalytic systems is a central component of every solar fuel scenario that proposes artificial photosynthesis as the basis for future energy security on a global scale.¹⁻³ Despite progress on synthetic systems,⁴⁻⁷ a realistic candidate for a robust artificial water oxidation catalyst on an industrial scale has yet to emerge. Thus, the natural water oxidizing system, the membrane-bound protein complex photosystem II (PSII) of plants, algae, and cyanobacteria, remains an invaluable source of information and inspiration, being a unique example of highly efficient light-driven water splitting. The oxygen evolving complex (OEC) of PSII contains a catalytically active oxo-bridged Mn_4Ca cluster that stores the four oxidizing equivalents required to oxidize water into dioxygen.⁸⁻¹² During catalysis the OEC passes through five oxidation states S_i of the Kok cycle,^{13, 14} where $i = 0-4$ denotes the number of oxidizing equivalents stored in each step (Figure 1). The S_2 and S_3 states are metastable and decay eventually to the dark-stable S_1 state,

whereas S_4 is a transient state that releases dioxygen and decays to S_0 . Although the Kok cycle rationalizes the period-four oscillation of flash-induced oxygen evolution via the sequential accumulation of four oxidizing equivalents, it does not place restrictions on the absolute oxidation states of the individual Mn ions and the protonation states of oxygen ligands that comprise the inorganic cluster. Although these latter questions are of fundamental importance for understanding the function of the natural system and for establishing the principles for the rational design of synthetic water splitting systems, they have remained contentious even after decades of intense research.^{8, 12, 15}

Historically, two competing schemes have been developed to describe the sequence of the Mn oxidation events within the catalytic cycle. They initially evolved from electron paramagnetic resonance (EPR) spectroscopy, which demonstrated that the S_2 state EPR multiline signal, which represents a total effective $S = 1/2$ spin ground state, is formed by the magnetic coupling of Mn(III) and Mn(IV) ions.¹⁶⁻²²

Since the OEC contains four Mn ions, this leads to two equally reasonable oxidation state assignments for the S_2 state that differ by two in their total valence electron count, $\text{Mn(III)}_3\text{Mn(IV)}$ and Mn(III)Mn(IV)_3 .¹⁸ As it is known from EPR and X-ray spectroscopy studies that the relative oxidation level of the OEC tracks the oxidation events of the catalytic cycle,^{17, 23-27} these two possible oxidation state distributions for the S_2 state can be extended to all other S states. The two resulting schemes (Figure 1) are usually referred to in the literature^{15, 28} as the low and high oxidation state paradigms or the low-valent (LV) and high-valent (HV) schemes. Although EPR results by different groups have been interpreted in support of either the LV^{29, 30} or the HV schemes,³¹⁻³⁴ unambiguous assignments of the ground state spin multiplicity³⁵ of all S_i states have been made: $S = 1/2$ (S_0),³⁶⁻³⁹ $S = 0$ (S_1),^{40, 41} $S = 1/2$ and $5/2$ (S_2 , $g = 2$ and $g \geq 4.1$ signals),^{16, 42, 43} and $S = 3$ (S_3),⁴⁴⁻⁴⁶ and these studies often provide information on low-lying excited states.

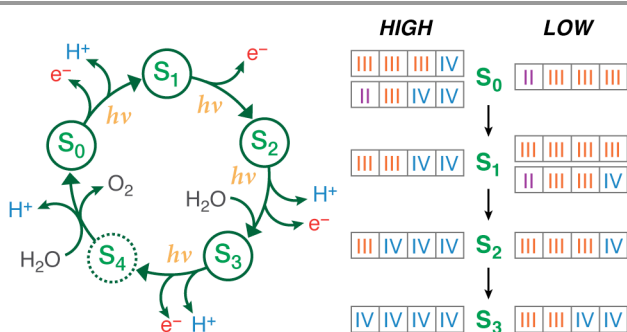


Figure 1. Left: the Kok cycle of S states, indicating the oxidation and proton release events at each transition. Right: the possible formal oxidation states of the four manganese ions of the OEC in the S_0 - S_3 states according to the high-valent and low-valent schemes.

Experimental approaches used to establish the absolute Mn oxidation states of the OEC fall broadly into four categories: i) photoassembly studies of the functional cluster starting from Mn(II) , ii) treatments that involve reduction of the OEC and study of the super-reduced states or titration of released Mn(II) , iii) experiments focusing on the kinetics of ^{18}O exchange, and iv) spectroscopic studies that probe the geometric and electronic structure of the functional enzyme. Divergent conclusions have been reached from the above approaches. For example, by determining the number of light flashes required to construct functional O_2 -releasing OEC from apo-OEC-PSII and Mn(II) , the LV scheme was favored.⁴⁷⁻⁴⁹ However, studies determining the amount of reductant required to disassemble a specific S state with concurrent titration of released Mn(II) ⁵⁰ or probing the reduced S states instead support the HV $\text{Mn(III)}_2\text{Mn(IV)}_2$ assignment for the S_1 state.⁵¹ $\text{H}_2^{16}\text{O}/\text{H}_2^{18}\text{O}$ substrate water exchange experiments⁵²⁻⁵⁴ have been interpreted in favor of both the LV scheme^{15, 55} and the HV scheme.^{56, 57} It is noted that the connection between water exchange rates and Mn coordination geometries or oxidation states remains ambiguous for the OEC.

X-ray spectroscopies^{17, 58, 59} provide complementary electronic structure information to that obtained by EPR, from the near-edge region of the metal K-edge X-ray absorption spectrum (XANES, X-ray absorption near edge spectroscopy), and geometric structure information, i.e. metal–ligand and metal–metal separations and coordination numbers from the EXAFS region (extended X-ray absorption fine structure). Oxidation states have been inferred from XANES spectra via calibration against model compounds. All experimental groups have concluded that their data provide support for the HV scheme,^{24, 26, 27, 60-62} but a subsequent report has reinterpreted these data to be in better agreement with the LV scheme.²⁸ For the experimentally based evaluation of S state dependent changes, ambiguities exist on how to best determine the edge position.^{24, 61, 62} These uncertainties originate in part from the dependence of the XANES spectral shape on ligand type and coordination environment. Nevertheless, a consensus exists among the EXAFS groups that a Mn-centered oxidation take place in both the S_0 - S_1 and S_1 - S_2 transitions (see however⁶³). For the S_2 - S_3 transition both a ligand-centered oxidation^{24, 27, 64, 65} and a Mn-centered oxidation^{23, 61, 62, 66} are supported by different groups. The use of X-ray emission spectroscopy (XES) has been rather limited, but the available data on Mn K β main lines has been interpreted as being consistent with the HV assignment in the S_1 state.²⁴

Computationally, various S state models of the OEC have been studied in both the high⁶⁷⁻¹⁰³ and the low¹⁰⁴⁻¹⁰⁹ valent schemes. It is useful to distinguish between computational models compatible with the cluster nuclearity and connectivity of the crystallographic structure at 1.9 Å resolution,¹¹⁰ and those developed before this information was available; for example, some of the early LV models feature four oxo bridges instead of the five identified in the most recent crystal structure.¹¹⁰ The lower number of oxo bridges (four) favors a lower overall oxidation level.¹⁰⁵ Although the 1.9 Å crystal structure clarifies the connectivity of the protein with the inorganic cluster, it features unusually long Mn–Mn and Mn–O bond lengths that are inconsistent with EXAFS data and indicate photoreduction of the Mn ions^{111, 112} to oxidation states that are non-physiological within either the HV or the LV scheme.^{11, 90, 113} A recent study by Suga et al.¹¹⁴ using femtosecond X-ray pulses from a free-electron laser (XFEL) provided a 1.95 Å resolution structure of the OEC that confirms the presence of radiation damage in the 1.9 Å XRD model¹¹⁰ and agrees better with EXAFS. Overall, however, in view of the above considerations and the ability to provide state-specific structural information, EXAFS appears as the more reliable and useful dataset for intermetallic distances within the OEC.^{62, 115-121}

Here, we aim to provide a comprehensive comparison of the two competing oxidation state schemes using a common structural framework and methodological approach. Large computational models were constructed for all stable S states (S_0 - S_3) in both the HV and the LV schemes and their properties were evaluated against experimental data on the geometry, electronic structure and spectroscopic properties of the OEC.

The present work is built upon methods that have been extensively benchmarked and shown to always correctly predict the ground state spin multiplicities of spin-coupled manganese complexes, and to be highly discriminative for other spectroscopic parameters.¹²²⁻¹²⁷ Additionally, new ⁵⁵Mn Davies ENDOR spectra obtained at 2.5 K are reported for the S₂ state of the OEC. It is demonstrated that only the high-valent scheme leads to a formulation of the catalytic cycle that is consistent with spectroscopic observations for each individual S state, and internally consistent in terms of catalytic S state progression.

METHODOLOGY

Construction of Models

Computational models are based on the protein pocket described in the XRD model of PSII at 1.9 Å resolution,¹¹⁰ which is practically identical with the 1.95 Å resolution XFEL model.¹¹⁴ The inorganic core is composed of four Mn ions and one Ca ion, oxo/hydroxo bridges and four water-derived ligands (see Figure 2 for the labeling scheme employed). Amino acids directly coordinating Mn ions (from the D1 protein unless stated otherwise) are His332, Glu189, Asp342, Ala344, CP43-Glu354, Asp170, and Glu333. Second-sphere residues include His337 (H-bond with O3), CP43-Arg357, Asp61 (H-bond with the Mn4-bound W1), the redox-active Tyr161 (Y_Z), and His190. Eight crystallographic water molecules involved in hydrogen bonding are included (HOH IDs from the 3ARC PDB structure: 358, 428, 442, 446, 538, 539, 542, and 923). Specific interactions between the first and second coordination sphere are maintained by including the backbones of Ser169, Leu343, and part of Gly171. Sets of possible HV and LV models were optimized for each S state examining various proton distributions among titratable groups, varying the starting electronic structure to explore different oxidation state arrangements and Jahn–Teller axis orientations of the Mn(III) ions, testing alternative side chain rotations of non-coordinating residues, and, in the case of the S₃ state, the inclusion of an additional water-derived ligand.

Having already examined in detail^{93, 94, 97-99, 102} the question of required second-sphere residues, we have identified two preconditions for the reliable development of models and the meaningful discussion of their properties: i) regardless of the total size of a model, it is necessary to include all hydrogen-bonding interactions with first sphere ligands (e.g. with Asp61) to prevent errors in the prediction of protonation states and oxidation state distributions, and ii) inclusion of the Tyr161–His190 pair is crucial in order to avoid geometric and electronic structure artifacts such as extensive rearrangement of water molecules around Ca²⁺, energetic bias towards specific conformations of the inorganic core and changes of the intrinsic redox balance of this tightly coupled system.¹⁰²

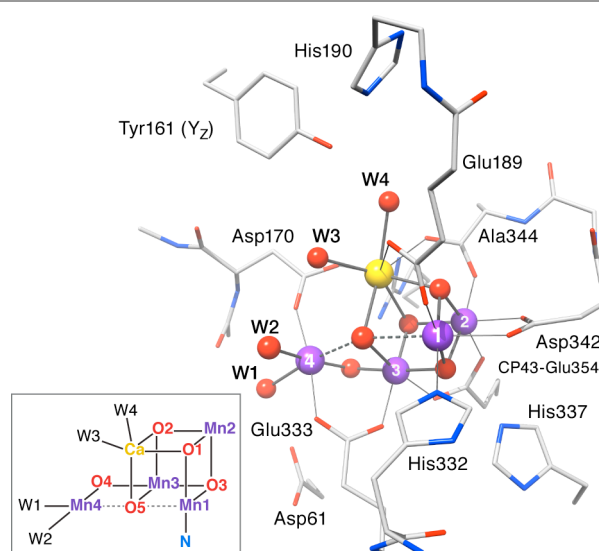


Figure 2. The inorganic core of the OEC from the 2011 X-ray structure of PSII¹¹⁰ with parts of the protein environment that are included in the present models; hydrogen atoms and non-coordinating waters are omitted for clarity. The labeling conventions used in this work are indicated in the inset.

Screening Criteria

In addition to energy-based evaluation of the models, the ground state multiplicity of the intermediates is used as an important experimental criterion (Table 1).³⁵ Geometric evaluations are based on comparison with intermetallic EXAFS-derived distances. Over the past decade, a consistent picture of Mn–Mn distances has been reached by EXAFS,^{62, 115-121} with three¹²⁸ (or two in S₀ to S₂)^{62, 129} short Mn–Mn distances of less than 2.8 Å in each S state and one (or two in S₀ to S₃)^{62, 129} long Mn–Mn distance of ca. 3.3 Å. The long Mn–Mn distance is less well-resolved due to its overlap with two to four Mn–Ca vectors¹³⁰⁻¹³² of similar length, so we only use the short Mn–Mn distances as a criterion for model discrimination (Table 1). As stressed above, comparison with crystallographic distances is not as informative because of photoreduction of the Mn ions in the 1.9 Å XRD structure.^{111, 112} This is demonstrated by the recent 1.95 Å XFEL structure of the OEC,¹¹⁴ which is characterized as “radiation-damage-free” owing to the femtosecond duration of the pulses. It has two Mn–Mn distances close to 2.7 Å, one close to 2.9 Å, and a longer one at 3.2 Å in better agreement with the EXAFS data for the S₁ state.

Table 1. Ground state spin *S* and short Mn–Mn EXAFS distances *R* (Å) collected from Ref. 120 (“Berkeley”) and Refs. 62, 116, 133 (“Berlin”) for the S₀–S₃ states of the OEC.

state	<i>S</i>	<i>R</i> _{Berkeley}	<i>R</i> _{Berlin}
S ₀	1/2	2.68, 2.77, 2.77	2.7, 2.8
S ₁	0	2.71, 2.71, 2.79	2.7, 2.7
S ₂	1/2, 5/2	2.74, 2.74, 2.74	2.69, 2.74
S ₃	3	2.75, 2.75, 2.79	2.73, 2.73, < 2.77

Similar sets of ^{55}Mn hyperfine coupling constants (HFCs) for the S_0 and S_2 states have been reported by different groups.^{31, 32, 134} For the S_3 state ^{55}Mn HFCs were also obtained recently.⁴⁶ These are presented in the corresponding sections (Tables 2 and 3). Selected models from each oxidation state scheme are also evaluated in terms of their Mn K pre-edge spectra, using the pre-edge region of published XAS spectra²⁴ as reference.

Computational Details

All calculations were carried out with ORCA.¹³⁵ Scalar relativistic effects were included with the ZORA Hamiltonian.¹³⁶⁻¹³⁹ For geometry optimizations the dispersion-corrected¹⁴⁰ BP86 functional^{141, 142} was used with ZORA-recontracted¹⁴³ TZVP (Mn, Ca, O, N) and SVP (C, H) basis sets.¹⁴⁴ Fully decontracted def2-TZVP/J auxiliary basis sets¹⁴⁵ were used for the Coulomb density fitting approximation. Selective backbone constraints were applied (see Figure S1). The COSMO model with $\epsilon = 8$ was used self-consistently in optimizations.¹⁴⁶ Tight SCF convergence and increased angular and radial integration grids were used (“Grid6” and “IntAcc 6.0”, respectively, in ORCA nomenclature). Broken-symmetry (BS) calculations for the exchange coupling constants were performed with the TPSSh functional¹⁴⁷ using the RIJCOSX approximation.¹⁴⁸ Convergence to the correct determinant was confirmed by the atomic spin populations, which are always close to the ideal values for high-spin Mn ions (see SI). Singular value decomposition was used to determine the exchange coupling constants J_{ij} , followed by diagonalization of the Heisenberg Hamiltonian to obtain the full spectrum of spin eigenstates. The methodology has been used successfully for many exchange-coupled Mn systems.^{46, 92, 94, 97, 122, 123, 125, 127} In the SI, we provide results for additional calculations performed in the course of this work on synthetic complexes: in all reported examples of spin-coupled Mn complexes, the approach correctly predicts the ground state spin multiplicity.

The lowest-energy BS determinant was used for calculating ^{55}Mn hyperfine coupling constants, which were projected using previously described protocols.^{93, 122} TPSSh calculations used increased radial integration grids for Mn centers. A complete mean-field approach was used for spin-orbit coupling; “picture-change” effects arising from the use of the scalar relativistic Hamiltonian were also included. Mn K pre-edge spectra were obtained with time-dependent DFT calculations within the Tamm–Dancoff approximation, using the TPSSh functional and def2-TZVP(-f) basis sets. The reference wave function was the lowest-energy BS solution. Other settings followed a recent calibration study.¹⁴⁹ The donor space was constrained to Mn 1s orbitals and each donor ion was treated in a separate calculation of lowest 100 roots. The acceptor space contained all unoccupied orbitals. The calculated intensities include electric dipole, magnetic dipole and electric quadrupole excitations. To facilitate comparison with experiment, individual transitions were broadened by 1.5 eV and a shift of 36.3 eV was applied.¹⁴⁹

EPR Experimental Details

The PSII core complex preparations were prepared from *T. elongatus* mutant which lacks the TyrD residue.¹⁵⁰ The chlorophyll concentration was ca. 3 mg/ml. The samples were placed in Q-band (1.6 mm I.D.) quartz tubes. After dark-adaptation for one hour at room temperature, the samples were given one pre-flash using a YAG laser (532 nm) and again placed in the dark for one hour at room temperature. PpBQ (2-phenyl-p-benzoquinone) dissolved in DMSO (dimethyl sulfoxide) was then added to the tube (0.5 mM final concentration) and the sample was given one light flash using a YAG laser (532 nm) and immediately cooled in a dry ice/ethanol bath (200 K) and then into liquid nitrogen.

Q-band pulse EPR and ^{55}Mn -ENDOR measurements were performed at 2.5 K and 5.0 K using a Bruker ELEXSYS E580 Q-band pulse EPR spectrometer equipped with a home-build TE₀₁₁ microwave resonator¹⁵¹ and a Cryogen Free Variable Temperature Cryostat from Cryogenic Ltd. Electron spin echo-detected (ESE) field-swept spectra were measured using the pulse sequence: t_p-t-2t_p-t -echo. The length of the $\pi/2$ microwave pulse was generally set to $t_p = 16$ ns. The interpulse distance was set to $t = 260$ ns. Electronic T_2^* relaxation was assessed by monitoring the intensity of the EPR signal (echo) as a function of the interpulse distance t . The decay of the EPR signal was approximately mono-exponential. ^{55}Mn -ENDOR spectra were acquired using the Davies-type pulse sequence: $t_{inv}-t_{RF}-T-t_p-t-2t_p-t$ -echo using an inversion microwave pulse of length $t_{inv} = 32$ ns, and a radio frequency (RF) π pulse of length $t_{RF} = 3.5-4.0$ μs . The length of the $\pi/2$ microwave pulse in the detection sequence was generally set to $t_p = 16$ ns and the interpulse delays to $T = 1.5$ μs and $\tau = 260$ ns. The RF frequency was swept between 30–400 MHz.

Electronic longitudinal (T_1) relaxation was assessed using two methods: i) a Davies type three pulse sequence ($t_{inv}-T-t_p-t-2t_p-t$ -echo, i.e. inversion recovery); and ii) a Mims type three pulse sequence ($t_p-t-t_p-T-t_p-t$ -echo, i.e. stimulated echo decay). For both methods the decay of the EPR signal (echo) is monitored as a function of the interpulse delay (T). The second pulse sequence has the advantage in that it monitors the decay of the EPR signal due to both the T_1 relaxation and spectral diffusion i.e. T_1^* , both of which limit Davies ENDOR effect.¹⁵² The longitudinal decay of the EPR signal was approximately bi-exponential. A description of test measurements and calibration of the B_2 (RF) field with a mixed valence bis- μ -pivalato- μ -hydroxo bridged $\text{Mn}^{\text{II}}\text{Mn}^{\text{III}}$ model complex¹⁵³ (“PivOH”) is given in the Supporting Information.

RESULTS AND DISCUSSION

In the presentation of models, we first discuss the spectroscopically best-characterized S_2 state, for which new EPR data are also reported. Then we proceed to the next S state, the S_3 state. Finally, having screened major structural and electronic possibilities, we move to the S_1 and S_0 states. Evaluation of models is based on the criteria specified in section 2.2. To aid presentation and discussion of results, only a

selected subset of models that were studied and screened for a given oxidation scheme and S_2 state are presented, along with their major isomeric forms.

S_2 State High-Valent Models

Computational high-valent S_2 -state models that are consistent with the most recent crystallographic model of PSII have been presented before, both as part of theoretically derived proposals for the water oxidation mechanism^{71, 73, 154} and as the basis for explaining and interpreting a range of spectroscopic and kinetic observations,^{72, 91, 92, 94, 97} including the effects of $\text{Ca}^{2+}/\text{Sr}^{2+}$ substitution⁹⁵ and interaction with substrate analogs like NH_3 .^{98, 100, 155} Models of the same size, with the same amino acid residues and treated at the same level of theory, as the ones used in the present study can also explain the two interconvertible S_2 state EPR signals at $g = 2.0$ and $g \geq 4.1$.⁹⁷ These models, represented here by the **S₂H-1a/b** pair, have unprotonated oxo bridges, one terminal water in the form of H_2O (W1) and one in the form of OH^- (W2). These are designated as “three-proton models” because they have three protons distributed among the titratable groups O4, O5, W1 and W2. The lowest energy “open-cubane” isomer, **S₂H-1a**, contains the unique Mn(III) ion at Mn1 and has a ground state spin of $S = 1/2$, whereas in the “closed-cubane” form **S₂H-1b**, with an $S = 5/2$ ground state, the Mn(III) ion is positioned at Mn4. **S₂H-1a** has very close correspondence to the most recent S_2 state model proposed by Siegbahn (RMSD of the Mn positions from Ref⁷³ is only 0.040 Å), although the precise orientations of some first and second sphere amino acid residues differ between the models from that study and those presented by us here and previously.^{97, 99} Most obvious are the different rotations of the imidazole ring planes of His332 and His337, which in the present models follow the orientations of the crystallographic model.¹¹⁰ Although rotation of these residues was shown to have only minor energetic effects on the computed mechanism,⁷² this is not the case for spectroscopic properties: as demonstrated recently, the orientation of His332, which is dictated by a hydrogen bonding interaction with the second-sphere Glu329 residue, has a large influence on the HFC of the Mn1 ion to which it is coordinated.⁹⁹

A previous theoretical study showed that protonated oxo bridges are inconsistent with measured ⁵⁵Mn HFCs.⁹⁴ This conclusion, corroborated by later studies focusing on different properties,^{156, 157} is consistent with the absence of large proton couplings as assessed by ¹H-ENDOR.^{158, 159} Results presented here further support this thesis. Structures where O5 is protonated (**S₂H-3**, see Figure S4) are destabilized by more than 16 kcal mol⁻¹ relative to the isomeric form **S₂H-2a**. However, models with a higher proton count exist in the literature^{78, 82, 84, 89} and such “four-proton models” are also investigated here for completeness. When $\text{W1} = \text{W2} = \text{H}_2\text{O}$ (**S₂H-2a/b**) the energy difference between the open and closed-cubane forms is the same as for the **S₂H-1** pair. All S_2 H models (Figure 3) have similar metal–metal distances and are consistent with the three short and one long Mn–Mn distances derived from EXAFS.^{115, 120}

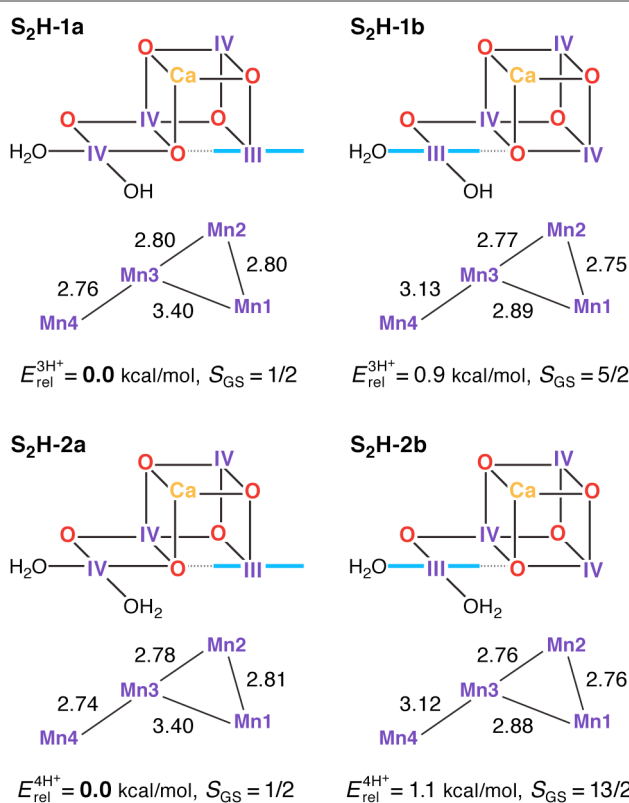


Figure 3. Protonation patterns, oxidation states, Mn–Mn distances (Å), relative total energies (kcal mol⁻¹), and ground spin states for the S_2 H models. Blue lines indicate the orientation of Jahn–Teller axes. The superscripts (3H⁺ and 4H⁺) indicate the total number of protons assigned to the groups W1, W2, O4, and O5, and serve to separate the models into isomer subsets for meaningful energy comparisons.

Although **S₂H-2a** exhibits the same desirable ground and first excited states ($S = 1/2$ and $3/2$, respectively) and energy gap as **S₂H-1a**, the corresponding closed cubane form **S₂H-2b** has a ground state of maximum spin multiplicity ($S = 13/2$ instead of $S = 5/2$) because the antiferromagnetic exchange interaction between Mn3 and Mn4 (J_{34}), is significantly diminished in **S₂H-2b** as compared with **S₂H-1b** (Table S1). Since the four-proton **S₂H-2** models cannot fit both EPR signals of the S_2 state, the **S₂H-1** couple with $\text{W2} = \text{OH}^-$ remains the preferred description of the S_2 state in the HV scheme.^{94, 97}

⁵⁵Mn hyperfine coupling constants serve as an independent means to evaluate the proposed models. Due to the structural and electronic similarities between **S₂H-1a** and **S₂H-2a**, the HFCs for the models are similar in magnitude. As shown before for models of this type,^{92-95, 99, 100} the predicted ⁵⁵Mn HFCs agree well with the experimental values (see Table 2).

Table 2. Calculated projected ^{55}Mn hyperfine coupling constants for selected S_2H and $\text{S}_0\text{H}/\text{S}_2\text{L}$ models and experimental values (decreasing absolute values, in MHz) for the multiline signals of the S_2 and S_0 states. Superscripts in brackets indicate assignments to Mn ions for the computational models.

	$^{55}\text{Mn } A_{\text{iso}} $			
S₂H-1a	295 ^[4]	223 ^[1]	209 ^[2]	185 ^[3]
S₂H-2a	303 ^[4]	227 ^[1]	204 ^[2]	201 ^[3]
S₀H-1a / S₂L-1a	264 ^[4]	227 ^[3]	223 ^[1]	214 ^[2]
S₀H-1c / S₂L-1c	313 ^[3]	308 ^[1]	249 ^[4]	247 ^[2]
S₀H-3a / S₂L-3a	266 ^[4]	204 ^[3]	199 ^[2]	144 ^[1]
S₂L-6	280 ^[1]	207 ^[2]	181 ^[4]	90 ^[3]
Exp. S₂ (Ref. ³¹)	298	248	205	193
Exp. S₂ (Ref. ³²)	297	245	217	200
Exp. S₂ (Ref. ¹³⁴)	324	255	238	191
Exp. S₀ (Ref. ³¹)	347	247	220	193

^{55}Mn -ENDOR of the S_2 state of the $\text{Mn}_4\text{O}_5\text{Ca}$ cofactor at 2.5 K

The ^{55}Mn hyperfine coupling estimates described above are derived from Davies ENDOR (see Fig. 4).^{31, 32, 134} In such experiments ^{55}Mn ENDOR transitions are observed over a relatively narrow frequency range, as compared to simpler model complexes, requiring all four Mn ions to display a similar hyperfine coupling in the coupled (measured) representation, i.e. of about 200–250 MHz. A recent experimental report though has thrown doubt on these results. Jin et al.³⁰ have repeated the ^{55}Mn ENDOR experiment on spinach PSII but now at much lower temperatures (2.5 K). In contrast to all previous literature studies, they observed a broader, structured ^{55}Mn ENDOR signal envelope interpreted as representing at least one ^{55}Mn hyperfine tensor of large anisotropy. This broad envelope was assigned as a signature of more than one Mn(III) ion, i.e. in support of the low-valent scheme, and as evidence for a dimer-of-dimers like magnetic coupling topology. The authors suggested that such ENDOR signals may have been obscured in earlier measurements at higher temperatures (5 K) due to enhanced nuclear relaxation. This surprising finding prompted us to repeat EPR/ENDOR measurements of S_2 state preparations from *T. elongatus* at the same low temperatures (2.5 K) using a new closed-cycle helium cryostat available from Cryogenic Ltd (see SI for details). The system was calibrated using a bis- μ -pivalato- μ -hydroxo Mn(II)Mn(III) model complex (“PivOH”)¹⁵³ previously described by Cox et al. (Figure 4B, details in the SI).¹⁶⁰

A control ^{55}Mn -ENDOR spectrum of the Mn_4CaO_5 cofactor in the S_2 state collected at 5 K is shown in Figure 4. It is seen to be very similar to previously published data, see Cox et al.⁹⁵ and Lohmiller et al.¹⁰⁰ Importantly, ^{55}Mn -ENDOR signals are only observed over a narrow radio frequency range, requiring all four Mn ions to display a similar hyperfine coupling, in line with a tetramer-like magnetic coupling topology.^{31, 32, 161} At this temperature, electronic T_1 relaxation ($T_1^* = 21 \mu\text{s}$) is sufficiently slow that a near full inversion of the spin echo is maintained during the Davies pulse sequence ($\approx 6 \mu\text{s}$), but is

sufficiently fast to allow efficient data collection, with repetition rates of the order of 1 ms. Subsequently, the sample was cooled to 2.5 K and the ^{55}Mn -ENDOR spectrum was re-measured. At this temperature, the T_1 time is at least ca. 2 ms, hampering data collection. Nevertheless ^{55}Mn -ENDOR data at a comparable signal to noise ratio could be obtained. It is readily observed that the ENDOR spectrum is essentially identical to that seen at 5 K, as expected (see Figure 4C). Data were collected at two repetition rates, 20 ms (saturating) and 250 ms. The spectra are the same using both data collection rates, however the 20 ms spectrum has a significantly better signal-to-noise ratio owing to the tenfold increase in the number of collected averages. It is noted that the relaxation time at 2.5 K (2 ms, 500 s^{-1}) is now in the range where the authors of Jin et al. hypothesize that additional ^{55}Mn -ENDOR signals should appear.³⁰ No such signals are observed in our study, hence we cannot confirm the observations made in the study of Jin et al.³⁰ The ^{55}Mn ENDOR data are instead consistent with a tetramer-like magnetic coupling topology, which results in all four Mn ions displaying similar hyperfine couplings.

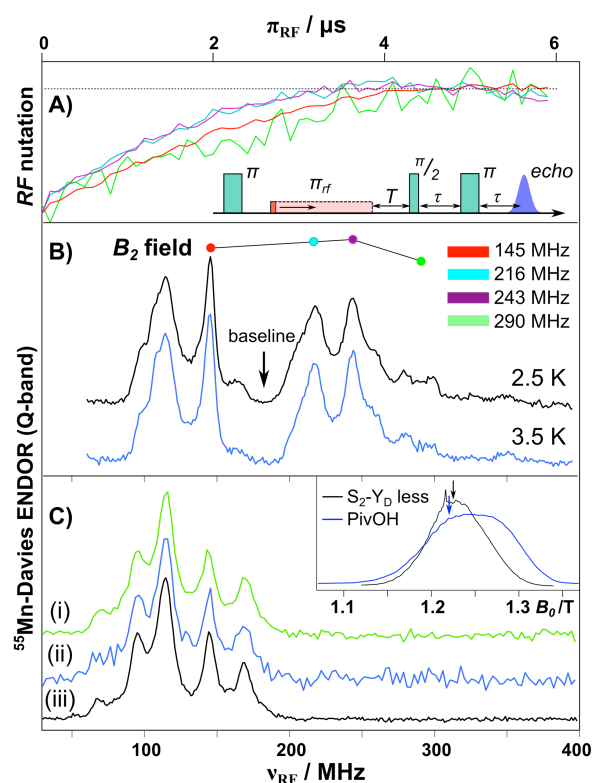


Figure 4. Q-band ^{55}Mn -Davies ENDOR of the Mn(II)Mn(III) PivOH complex and the S_2 (multiline) state of the $\text{Mn}_4\text{O}_5\text{Ca}$ cofactor isolated from *T. elongatus*. **A)** Normalized nuclear spin nutation curves measured at the positions marked in panel B demonstrating the linearity of the B_2 field over the 150–300 MHz range. A baseline nutation curve measured at 185 MHz was subtracted from each data trace. **B)** ^{55}Mn -ENDOR spectra of the PivOH complex measured at center field of the EPR spectral envelope (see inset in panel C). **C)** Q-band ^{55}Mn -Davies ENDOR of the S_2 state measured at center field of the EPR spectral envelope (see inset in panel C). The RF frequency was swept between 30 and 400 MHz in 1.2 MHz steps (at 5 K) or 2.5 MHz steps (at 2.5 K). Total data collection times were comparable: (i) 2.5 K (green), 20 ms repetition rate (ca. 18 hours); (ii) 2.5 K (blue), 250 ms rep. rate (ca. 17 hours); and (iii) 5 K (black), 1 ms rep. rate (ca. 14 hours).

S₃ State High-Valent Models

The transition from the S₂ to the S₃ state represents a single oxidation event.¹⁶² We have recently examined this oxidation in the context of the HV scheme,¹⁰² where it was observed that the *in silico* oxidation of S₂ state models leads to the formation of an S₂Y_Z[•] electronic state, that is, the one-electron oxidation of the Y_Z residue as opposed to the oxidation of a Mn ion or ligand in the OEC. These structures are considered good models for intermediate “split signal” states, which can be trapped experimentally by advancing the Kok cycle at low temperatures. It is noted that in smaller models, which do not include the Y_Z/His190 couple, this result is clearly absent demonstrating the importance of retaining this structural unit to correctly capture the energetics of the OEC. Reaching the S₃ state *in silico*, i.e. proceeding beyond the S₂Y_Z[•] state, thus requires modification of the cofactor. Experimental data suggest that the transition from the S₂ to the S₃ state is accompanied by the loss of a proton,¹⁶² and most probably also by the binding of an additional water molecule^{163, 164} that may not be the substrate in the present Kok cycle.^{54, 165} Inclusion of both of these chemical modifications (deprotonation and water binding) leads to the oxidation of the OEC and formation of the S₃ state. Note that a model where no additional water is bound to the Mn cluster, leading to a trigonal-bipyramidal coordination geometry of Mn4, is characterized by a spin ground state at variance with experimental data for the S₃ state (model S₃H-5, see SI).

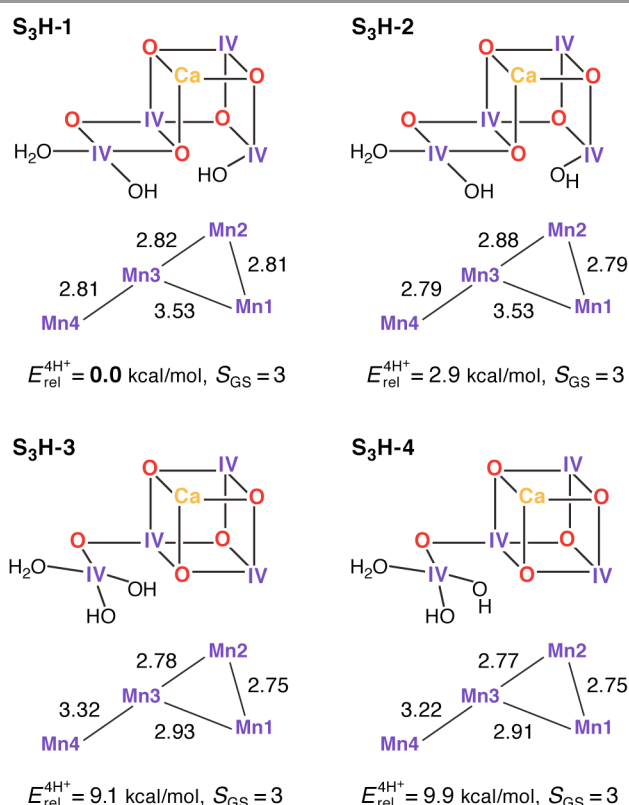


Figure 5. Protonation patterns, oxidation states, Mn–Mn distances (Å), relative total energies (kcal mol⁻¹), and ground spin states for four selected S₃H models.

Depending on the site of proton removal and the rearrangements that may take place prior to formation of the final S₃ state, either H₂O or OH⁻ can be added to the S₂-state models. The two S₂H models presented above suggest immediately two possible binding sites for the water molecule: the open coordination site of Mn1 for the open cubane S₂H-1a, and the open coordination site of Mn4 for its valence isomer S₂H-1b. After considering several protonation patterns, the energetically preferred models are those presented in Figure 5. The differences between S₃H-1/S₃H-2, derived from S₂H-1a, and S₃H-3/S₃H-4, derived from S₂H-1b, relate to the arrangement of hydrogen bonds, with the additional OH⁻ being H-bonded to O5 in S₃H-1 and S₃H-3, but not in S₃H-2 and S₃H-4. Importantly, the structures derived from S₂H-1a are significantly more stable than the ones derived from the closed cubane form S₂H-1b, a change from approximately 1 kcal mol⁻¹ in S₂ to almost 10 kcal mol⁻¹ in S₃.⁴⁶ As with the open-cubane structure of the S₂ state, the lowest-energy S₃H models correspond equally closely to models proposed by Siegbahn.⁷¹⁻⁷³ It is noted that there may be further structural intermediates between the S₂ and S₃ states (in addition to the split signal states described above) that facilitate the binding of the new water molecule; these sub-states are not considered in this study, since we aim here to characterize the stable catalytic intermediates.

All current interpretations of EXAFS data require the cofactor to contain three short Mn–Mn distances of up to 2.82 Å for S₃.^{62, 120} All S₃H models have at least two Mn–Mn distances shorter than 2.81 Å, model S₃H-1 has also a third short distance of 2.82 Å, whereas the third shortest distance for the other models is longer (2.88–2.93 Å). Thus, the lowest-energy isomer is also the one that matches EXAFS distance constraints most closely. An aspect controversially discussed in the literature concerns the possibility of ligand-centered versus metal-centered oxidation in the S₂–S₃ transition. In all S₃H models the unpaired spin density is localized on the Mn ions, which have spin populations close to 2.9 electrons, as expected for Mn(IV) ions with a high-spin d³ electron configuration. Spin density on ligating O or N atoms is insignificant and the O bridges never carry spin populations in excess of 0.15 electrons. Thus, the present models do not support ligand-centered oxidation.^{24, 27, 166} This is consistent with an interpretation of X-ray absorption spectra⁶² that suggested the S₂ to S₃ transition to be accompanied by a change in the coordination sphere of the Mn oxidized from five-coordinate Mn(III) in S₂ to six-coordinate Mn(IV) in S₃, as in the S₂H and S₃H models presented here.

The predicted ground state spin for all S₃H models is $S = 3$, consistent with experiment,^{45, 46} regardless of differences in metal–oxo connectivity. An additional criterion for the models arises from the ⁵⁵Mn hyperfine coupling constants.⁴⁶ These have recently been established to be isotropic, strongly suggestive of octahedrally coordinated Mn(IV) ions, a condition that is satisfied by all S₃H models presented here (see Table S9). Experimentally, the observed ⁵⁵Mn HFCs for S₃ fall into two classes (in terms of absolute magnitude): a) a large

coupling class, where the hyperfine interaction is larger than the nuclear Larmor frequency with $|A| \approx 100$ MHz, and b) a small coupling class, where the hyperfine interaction is smaller than the nuclear Larmor frequency with $|A| < 30$ MHz.⁴⁶ Importantly, the Mn ions of the large coupling class display *negative* ⁵⁵Mn HFCs whereas the Mn ions of the small coupling class display ⁵⁵Mn HFCs, which may be assigned as either positive or negative (for a full discussion see Cox et al.⁴⁶).

Table 3. Calculated projected ⁵⁵Mn hyperfine coupling constants (MHz) for S₃H and S₃L models and experimental values for the S₃ state, ordered high to low in terms of absolute values. Superscripts in brackets indicate assignments to Mn ions. Positive sign for the HFC identifies the Mn ion with β spin.

model	⁵⁵ Mn $ A_{iso} $			
S ₃ H-1	-86 ^[1]	-76 ^[2]	-34 ^[3]	27 ^[4]
S ₃ H-2	-99 ^[2]	-88 ^[1]	-29 ^[4]	20 ^[3]
S ₃ H-3	88 ^[4]	-81 ^[1]	-78 ^[2]	-70 ^[3]
S ₃ H-4	86 ^[4]	-79 ^[2]	-75 ^[1]	-65 ^[3]
S ₃ L-2	-94 ^[1]	-75 ^[4]	-74 ^[2]	53 ^[3]
S ₃ L-3	-105 ^[2]	98 ^[4]	-92 ^[1]	-79 ^[3]
S ₃ L-8	-94 ^[3]	-83 ^[4]	-74 ^[2]	49 ^[1]
S ₃ L-10	-100 ^[4]	-93 ^[1]	-80 ^[2]	60 ^[3]
Exp. (Ref. ⁴⁶)	-99.0 ^[1 or 2]	-95.6 ^[1 or 2]	-25.9 ^[3 or 4]	≤5 ^[3 or 4]

In polynuclear complexes such as the present systems, the ⁵⁵Mn HFCs are determined by two factors: a) the intrinsic site HFC values, which are predicted in this case to be within the narrow range 160–250 MHz for all models, similar to values for octahedral mononuclear Mn(IV) complexes and consistent with the identical oxidation state and similar coordination of all sites, and b) the spin projection coefficients, i.e. the local spin expectation values scaled by the spin ground state, which function as weighing factors that describe the contribution of each ion to the electronic manifold of interest. The spin projection coefficients thus reflect the magnetic coupling topology of the cluster. In terms of idealized coupling schemes, the two types of core connectivity (open and closed cubane, Figure 5), represent two limiting cases that both lead to a spin ground state of $S = 3$: a “dimer of dimers” topology with two weakly coupled subunits, a ferromagnetic Mn1-Mn2 ($S_{12} = 3$) and antiferromagnetic Mn3-Mn4 ($S_{34} = 0$) one, and a “trimer-monomer” topology where a trimeric $S_{123} = 9/2$ subunit couples antiferromagnetically with the $S_4 = 3/2$ outer Mn4. The spin projection coefficients for the latter case will be approximately equal, thus leading to approximately equal HFCs given similar site HFC values, whereas for the first case the spin projections will fall into two classes, large ones for the Mn1-Mn2 subunit and small ones for the Mn3-Mn4 subunit.⁴⁶

From the above discussion, it is expected that the open-cubane structures would be more suitable to yield the two different classes of ⁵⁵Mn HFCs required by experiment. This is seen in our calculations: for S₃H-1 and S₃H-2 the spin projection coefficients are [0.48, 0.44, 0.18, -0.11] and [0.47, 0.49, -0.08, 0.11] for Mn1–Mn4, whereas those for S₃H-3 and

S₃H-4 are [0.48, 0.46, 0.43, -0.37] and [0.47, 0.47, 0.44, -0.37]. Thus, models S₃H-1 and S₃H-2 reproduce the two classes of HFCs (Table 3), whereas S₃H-3 and S₃H-4 do not. The inclusion of the sign of the hyperfine as a constraint is unique so far and has not been achieved for any other S state. The calculated HFCs presented here show that the large hyperfine couplings are negative, in line with experiment. It is also noted that the spin topology in S₃H-1, S₃H-3 and S₃H-4 is $\alpha\alpha\alpha\beta$, while that in S₃H-2 is $\alpha\alpha\beta\alpha$, therefore both S₃H-1 and S₃H-2 reproduce additionally the experimental constraint regarding the possible sign reversal in one of the small HFCs. Numerical agreement between experimentally fitted and calculated HFCs for Mn3 and Mn4 can be improved by small perturbations of the non-nearest-neighbor J_{13} and/or J_{14} coupling pathways (± 2 cm⁻¹), which are the least well-defined computationally.

S₁ State High-Valent Models

Spectroscopic measurements demonstrate that the OEC can be advanced from the S₁ state to the S₂ state at cryogenic temperatures,^{167, 168} while EXAFS of the S₁ and S₂ states shows that the geometric changes in the S₁–S₂ transition are too small to be resolved. Both observations, in combination with electrochromic measurements and the pH-insensitivity of the transition,^{129, 169, 170} suggest that the two states differ only by a redox event; hence, models for the S₁ state should resemble the S₂ state models in terms of structure. Accordingly, we discuss here models derived from S₂H models either with the same protonation pattern or with W2/O5 proton translocation (see Figure 6).

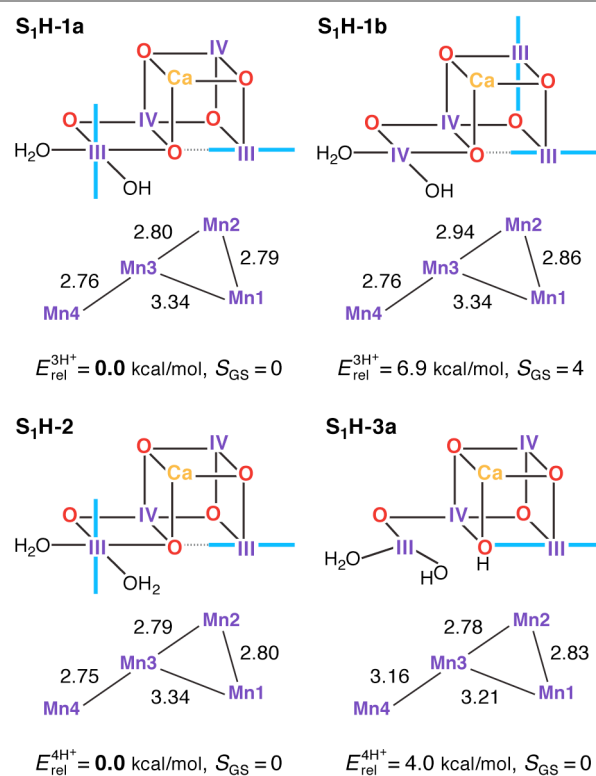


Figure 6. Protonation patterns, oxidation states, relative total energies and ground spin states for the S_1H models. Blue lines indicate the orientation of Jahn–Teller axes.

Two valence isomers derive from S_2H-1a/b (S_1H-1a and S_1H-1b), which differ not in the position of the oxo bridge O5, but instead in their oxidation state distribution. Specifically, in the lowest energy structure S_1H-1a , the two Mn(III) ions are located at the terminal Mn1 and Mn4 positions, whereas the higher energy structure (S_1H-1b) features two vicinal Mn(III) ions, at Mn1 and Mn2. This results in different exchange coupling pathways, with S_1H-1b displaying a ferromagnetic interaction between Mn1 and Mn2 (see Table S5). Combined with a reduction in the magnitude of the J_{34} antiferromagnetic coupling, as compared with S_1H-1a , this model ends up having an $S = 4$ ground state. All other S_1H models have a common III-IV-IV-III oxidation state distribution and display an experimentally consistent diamagnetic ground state.

Among the three-proton isomers, agreement with EXAFS is achieved only for the lower energy model S_1H-1a that contains three short Mn–Mn distances, whereas in S_1H-1b the corresponding distances are significantly longer. The core geometry of S_1H-1a agrees well with other computational high-valent S_1 state models.^{73, 78, 89} It is worth noting that whereas in the S_2 state the Mn(III) ion of either of the interconvertible S_2H minima features a Jahn–Teller axis oriented along Mn1–O5–Mn4, the Jahn–Teller axis of Mn4 in S_1H-1a is instead found to be oriented along Asp170 and Glu333. Therefore, since the σ -antibonding interaction is avoided, the nature of the Mn4–O5 bond in S_1H-1a should not be considerably different from S_2H-1a , despite the change in Mn oxidation state, which could be of relevance for the interpretation of substrate exchange.^{15, 31, 52, 54, 56, 69, 72, 98, 158, 171} Additionally, it would be worth exploring the implications for the interpretation of FTIR data on the S_1 – S_2 transition,^{172, 173} since the orientation of the Mn4 Jahn–Teller axis in S_1H-1a and its loss in S_2H-1a are expected to affect mostly the Asp170 and Glu333 carboxylate vibrational modes. Other HV literature models for the S_1 state suggest that both W1 and W2 could be present as H_2O ,⁷⁸ or that O5 and W2 could be OH^- groups.^{82, 84} The first proposal, represented here by S_1H-2 , leads to a model consistent with EXAFS⁷⁸ and spin-state constraints. In the case of the second suggestion, that is, with a protonated O5 bridge, only structures of the closed cubane type are stable, such as S_1H-3a . However, this model and its isomer S_1H-3b (Figure S4) are both higher in energy (4.0 and 6.4 kcal mol⁻¹, respectively) than the S_1H-2 alternative and both are inconsistent with EXAFS results (Table 1) due to a significant elongation of the Mn3–Mn4 distance. It is not possible to select one of S_1H-1a or S_1H-2 as the best model for S_1 , because both satisfy all constraints for this state in this study. Nevertheless, given that no change in protonation is expected between S_1 and S_2 , we favor the S_1H-1a model for reasons of consistency with the preferred S_2H model, S_2H-1a .

The structure of the cofactor reported in the 1.95 Å resolution XFEL model of PSII¹¹⁴ is also relevant to the question of the O5 protonation state. As with the EXAFS

reference, there is good agreement between the computed Mn–Mn distances of the plausible S_1H models reported above and the Mn–Mn distances of the XFEL model, with the exception of the Mn3–Mn4 distance that is reported a bit longer (ca. 2.9 Å) in the XFEL model. We also note that this study also agrees in the authors' tentative assignment of individual Mn oxidation states. The most obvious structural difference, however, is the Mn4–O5 bond length. Although the XFEL structure corrects the XRD model by placing the O5 close to Mn4 instead of in-between the Mn1 and Mn4 ions, the Mn4–O5 distance in the XFEL model is still long enough to lead the authors to suggest that O5 is present as a hydroxyl group. Given the evidence presented here regarding structural and spectroscopic consistency with the subsequent S_2 state, we consider this assignment unlikely.

Besides the possibility that the Mn4 ion may be sensitive enough to still suffer some photoreduction in the XFEL study, a more obvious reason for the structural inconsistency with the present models may lie in the preparation of the PSII samples used in that study. Specifically, long dark adapted PSII samples represent a 75%:25% mix of the S_1 and S_0 states, respectively.¹⁴ S -state synchronization requires a pre-illumination sequence described by Styring and Rutherford,^{174, 175} which relies on fast S_2 and S_3 deactivation to S_1 and slow S_0 oxidation by the tyrosine D residue. As this pre-illumination protocol was not performed for crystals used in the XFEL study of Suga et al., the reported structure may contain a non-negligible S_0 state contribution. As will be shown in the next section, O5 protonation is indeed most likely in the S_0 state, potentially explaining the elongation of the Mn4–O5 bond and its unusually high standard deviation reported for the XFEL structure.¹¹⁴

S_0 State High-Valent Models

In the S_0 – S_1 transition one electron and one proton are removed from the cluster.¹⁶² The proton can be lost from different sites in an S_0 model to form the expected S_1H-1a model: either of the O4 and O5 oxo-bridges that are unprotonated in S_1H-1a (yielding S_0H-1 and S_0H-2), or from W2, which would then be present as H_2O in S_0 (yielding S_0H-3). To further test the viability of the 4-proton models in S_1 and S_2 , 5-proton models for the S_0 state were also evaluated (S_0H-4 and S_0H-5). A dual labeling scheme is used in Figure 7, since most of these S_0H models serve also as models for the S_2 state in the low-valent scheme (S_2L).

Isomeric structures with different distributions of the same number of unpaired electrons among the four Mn ions are found for most protonation patterns. S_0H models with an oxidation state distribution III-III-IV-III are not compatible with EXAFS-derived Mn–Mn distances for the S_0 state, because the Jahn–Teller axis of Mn2 is always oriented along the Mn2–O3 bond resulting in longer Mn1–Mn2 and Mn2–Mn3 vectors. On the other hand, models with the oxidation state distribution III-IV-III-III have Mn–Mn distances that agree better with EXAFS and with the recent XFEL structure. The oxidation states are consistent with formal oxidation states

derived from ^{55}Mn -ENDOR.^{31, 161} An alternative to the (III)₃(IV) oxidation state assignment, i.e. (II)(III)(IV)₂, arises if the S_0 - S_1 transition involves a Mn(II)-Mn(III) rather than a Mn(III)-Mn(IV) oxidation. This possibility was left open in early EPR and XANES work,^{26, 36, 38, 176} but excluded in

subsequent ^{55}Mn -ENDOR studies.^{31, 161, 177} In the present models, a Mn(II) ion is found in the Mn4 position of **S₀H-3c** (see Figure S4) but in line with previous reports,^{82, 178, 179} it is strongly disfavored energetically by more than 23 kcal mol⁻¹ over its redox isomer **S₀H-3a**.

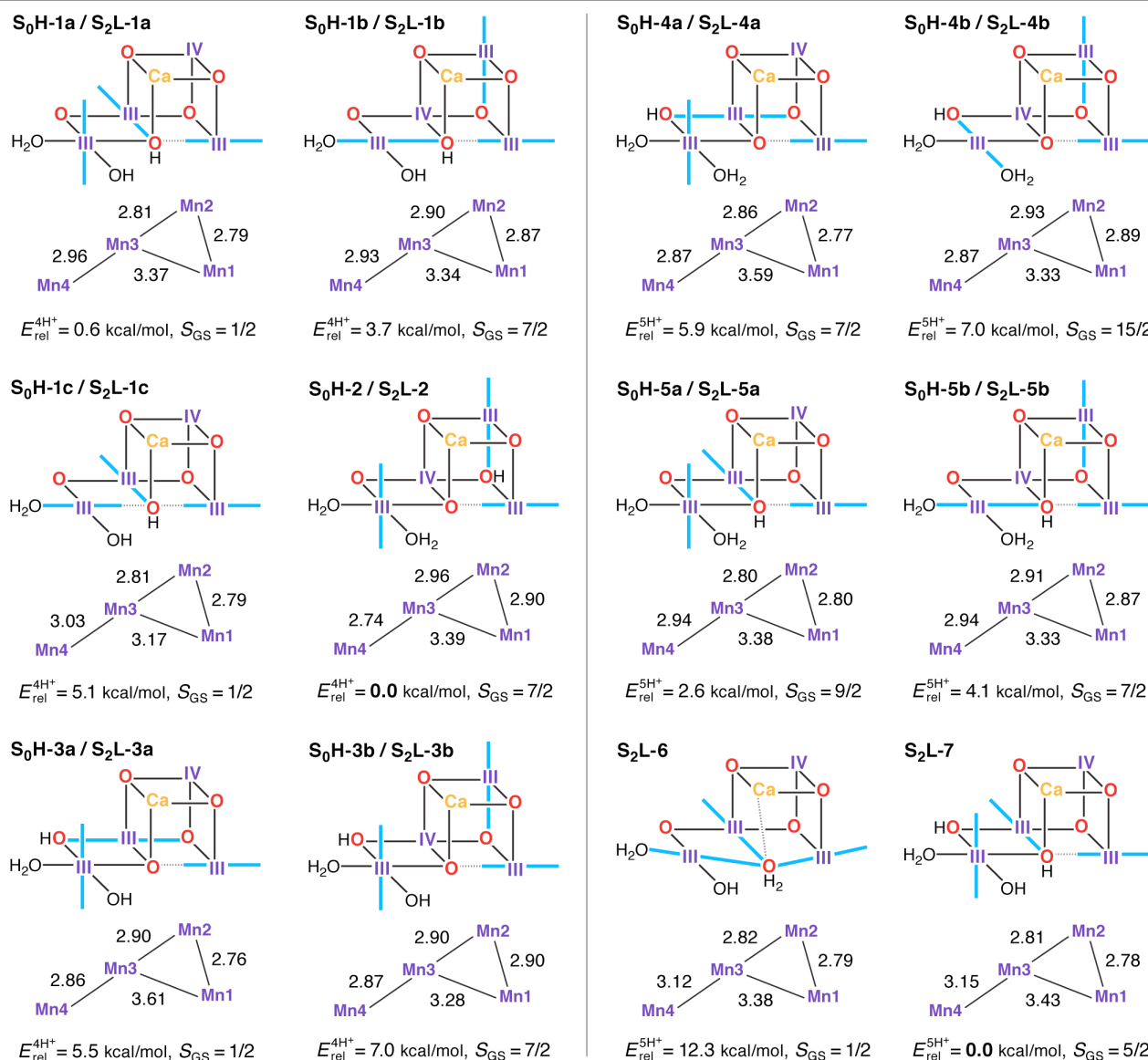


Figure 7. Protonation patterns, oxidation states, Mn–Mn distances (Å), relative total energies (kcal mol⁻¹), and ground spin states for the $S_0\text{H}$ and $S_2\text{L}$ models. Blue lines indicate the orientation of Jahn–Teller axes.

The spin state of S_0 is $S = 1/2$ for the multiline signal centered at $g = 2$, reproduced here by the four-proton models **S₀H-1a**, **S₀H-1c**, and **S₀H-3a**. Note that **S₀H-1a** and **S₀H-1c** differ mainly in the orientation of the Jahn–Teller axis of Mn4. Despite leading to the same ground spin state, the magnetic topologies of these three models differ qualitatively (see Table S4). The most pronounced difference concerns the nature of the J_{23} exchange coupling constant, antiferromagnetic in **S₀H-1a/1c** and ferromagnetic in **S₀H-3a**. The sign of J_{23} depends on the location of the Mn(IV) site and the Jahn–Teller axis orientations (Figure 7): ferromagnetic or weakly

antiferromagnetic interactions always arise between Mn(III) and Mn(IV) when the Jahn–Teller axis of the Mn(III) ion is oriented along a μ -oxo bridge between the ions. This is the case for the Mn2–Mn3 exchange pathway in the $S = 7/2$ models **S₀H-1b**, **S₀H-2**, **S₀H-3b**, **S₀H-4a** and **S₀H-5b**. The spin ground states of all 5-proton $S_0\text{H}$ models are $S \geq 7/2$, incompatible with experiment. These include models with a protonated O4 or O5 and W2 as a water molecule (**S₀H-4a/b** and **S₀H-5a/b**).

Models **S₀H-1a**, **S₀H-1c**, and **S₀H-3a** display first excited states of $S = 3/2$, at 2, 21, and 16 cm⁻¹, respectively. Since the separation between the ground and first excited state of S_0

reported in electron spin–lattice relaxation measurements (ca. 22 cm^{-1})¹⁷⁷ was obtained after treatment of PSII with methanol, which is known to increase this energy gap,^{31, 37, 180, 181} it is not obvious which model should be considered a better match in this respect. The relative energies of the three $S = 1/2$ models favor **S₀H-1a**, however it is noted that the relative energies of this model and its Jahn–Teller orientation isomer **S₀H-1c** display unusual sensitivity, unique among all HV models in this study, to the percentage of exact exchange in the density functional. Specifically, the energy difference of $4.5 \text{ kcal mol}^{-1}$ obtained with BP86 is reduced to practically zero with TPSSh (10% exact exchange) and is inverted to $-1.5 \text{ kcal mol}^{-1}$ with TPSS0 (25% exact exchange). This effect is presumably related to the different description afforded by different functionals of the energetic stabilization upon pseudo Jahn–Teller axis rotation at the Mn4 ion, thus complicating arguments based on energetics. In terms of computed ⁵⁵Mn HFCs, all $S = 1/2$ S₀H models agree less favorably with experimental values than the S₂H models. They all underestimate the largest ⁵⁵Mn HFC (Table 2) and in **S₀H-3a** the magnitude of the smallest HFC is additionally predicted too small. On the other hand, **S₀H-1c** overestimates the smallest HFC. Although there is room for improvement in modeling this state, either in terms of methodological refinement or in terms of additional input from experiment, overall we consider the general trends to be reproduced better by **S₀H-1a** or **S₀H-1c** (or both) than by **S₀H-3a**.

In summary, the results from the preceding sections on the high-valent scheme converge to the final sequence of models **S₀H-1a** → **S₁H-1a** → **S₂H-1a/b** → **S₃H-1**.

S₂ State Low-Valent Models

Although the high-valent option appears to be in full agreement with experimental constraints, it is important to investigate the LV options with the same rigor to make sure that the experimental constraints and analysis methods are indeed discriminative. Similar to the HV scheme, we start our analysis with the S₂ state, for which we use, as already suggested in previous literature proposals,^{107, 108} a higher total number of protons to compensate for the two additional electrons relative to the HV scheme, namely four or five protons distributed over O4, O5, W1 and W2. Most S₂L models (with the exception of the 5-proton forms **S₂L-6** and **S₂L-7**) are identical to the high-valent S₀ models presented in Figure 7.

The model that agrees best with EXAFS is the Mn(II)-containing **S₂L-3c** (see Figure S4), which has three Mn–Mn distances in the range 2.83–2.86 Å, but is excluded due to its very high relative energy of 24 kcal mol^{-1} . The best candidate S₂L models appear to be those that contain at most two Mn–Mn distances that can be classified as short. No S₂L model contains three short (i.e., $< 2.8 \text{ Å}$) Mn–Mn distances, and there is no obvious modification that would introduce an additional short distance. However, given the different EXAFS interpretations of the S₂ state (Table 1) and the documented tendency of a slight overestimation of Mn–Mn distances by DFT methods,⁷³

^{78, 80} we do not consider the Mn–Mn distance criterion conclusive enough to fully exclude the low-valent option.

Five of the LV S₂ models display one of the ground states observed experimentally: $S = 1/2$ for **S₂L-1a**, **S₂L-1c**, **S₂L-3a**, and **S₂L-6**; and $S = 5/2$ for **S₂L-3c** and **S₂L-7**. A key experimental observation that must be satisfied is the potential to interconvert between the low spin ($S = 1/2$) and high spin ($S = 5/2$) forms. Among the four-proton models, **S₂L-1a** is practically isoenergetic with the global minimum of the subset (**S₂L-2**), and thus we can consider it the best potential LV model for the $S = 1/2$ EPR multiline signal of the S₂ state. However, a problem arises when we consider possible 4-proton model candidates for the $S = 5/2$ EPR signal. Only one model, the Mn(II)-containing **S₂L-3c**, displays this ground state, but it is energetically inaccessible as pointed out above. These results make it hard to imagine a simple low-barrier interconversion for either of the $S = 1/2$ S₂L 4-proton models.

Among the five proton models a similar problem arises. **S₂L-6** resembles **S₂L-1c** in the orientation of the Jahn–Teller axes but differs in the protonation state of O5, present here as a loosely bound water. Note that this type of structure would be the corresponding S₂ state model of a low-valent S₁ state model proposed recently.¹⁰⁷ Our results indicate that **S₂L-6** could potentially explain the $S = 1/2$ species in terms of spin state, but it is strongly disfavored energetically. It is significantly higher in energy than its corresponding **S₂L-7** ($S = 5/2$) isomer and is, in fact, the highest-energy five-proton isomer of all models considered, with the energy difference separating it from the minimum-energy isomer increasing from 12 kcal mol^{-1} to over 18 kcal mol^{-1} with the use of hybrid functionals. Thus, in contrast to the high-valent, quasi-energetic and interconvertible **S₂H-1a/b** forms, no low-valent model set can explain the EPR phenomenology of the S₂ state in a similar complete way.

Additional information is provided by the ⁵⁵Mn HFCs for the models with $S = 1/2$ spin ground states. The experimental pattern of one HFC close to 300 MHz, one close to 250 MHz and two close to 200 MHz, is reproduced quite well by the high-valent S₂-state models (Table 2), but not as well by the low-valent models. **S₂L-1a**, **S₂L-3a** and **S₂L-6** predict relatively large hyperfine couplings as they display tetramer-like spin projections, but the projected HFCs are smaller than for the HV case because Mn(III) site HFCs are smaller than Mn(IV) site HFCs. Thus, a cluster with more Mn(III) ions will have smaller projected HFCs compared to a cluster with more Mn(IV) ions, assuming similar spin projections. **S₂L-1c** displays a different magnetic topology, resulting in HFCs that are uniformly too large. Among the present models, **S₂L-1a** shows the most reasonable agreement with experiment.

S₃ State Low-Valent Models

Several candidate S₃L models were constructed in an attempt to satisfy the criteria for the S₂–S₃ transition (Figure 8). In principle the S₁H models already described would represent candidates for S₃L, as seen for S₂L/S₀H. In this case however, it is already evident from their reported properties that there can be no agreement with experimental constraints for the S₃ state.

These models display neither the correct spin state ($S_{GS} = 3$) nor the correct Mn–Mn distances. Expanding upon this, S_3L models were constructed based on S_2L candidate structures which include an additional water ligand (H_2O/OH^-) as required for high valent S_3 state models (S_3H). Using S_2L-1 , S_2L-3 , S_2L-6 , and S_2L-7 as starting points, seven five-proton models and five six-proton S_3L models were constructed (Figure 8). The core geometry of S_3L-1 features three reasonably short Mn–Mn distances (2.80–2.85 Å) and can be thus considered consistent with EXAFS within DFT accuracy. The other models show at most two such distances, at variance with all interpretations of

EXAFS data for the S_3 state.^{62, 117, 120, 129} S_3L-1 is also the lowest-energy structure for the five-proton isomers. However, it has to be excluded as a candidate for the S_3 state because it is diamagnetic, with a large energy difference between the ground and first excited $S = 1$ state (Table S5). The correct $S = 3$ ground state is seen for two five-proton models S_3L-2 and S_3L-3 , but they are both higher in energy than S_3L-1 and disagree with EXAFS. Two of the six-proton models, S_3L-8 and S_3L-10 , also have the correct ground state. S_3L-8 is by far the lowest energy isomer in its subset, but fails to satisfy the requirement of three short Mn–Mn distances.

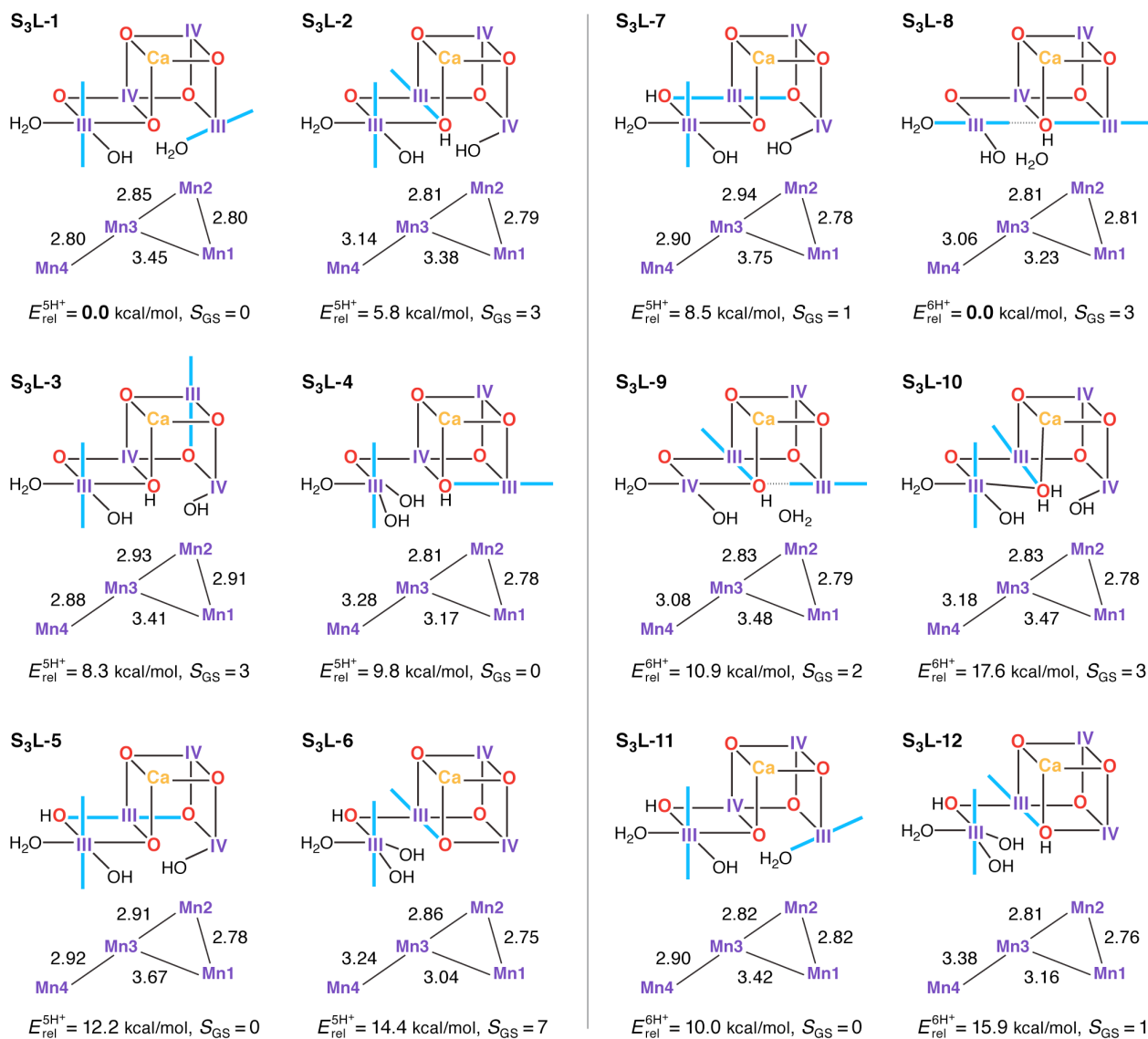


Figure 8. Protonation patterns, oxidation states, Mn–Mn distances (Å), relative total energies (kcal mol^{-1}), and ground spin states for the S_3L models. Blue lines indicate the orientation of Jahn–Teller axes.

The calculated ^{55}Mn HFCs provide additional evidence in the case of the S_3L models. Table 3 lists computed values for all models with an $S = 3$ ground state. Crucially, no S_3L model can reproduce the two classes of ^{55}Mn HFC observed experimentally,⁴⁶ thus providing a further argument against the

LV scheme. Additionally, no S_3L model satisfies the requirement for all Mn ions having isotropic HFCs, as shown by the anisotropic values listed in Table S8. Overall, despite individual S_3L models satisfying one or more of the constraints related to the S_3 state of the OEC, there is no single S_3L model

among the ones studied here that is consistent with all geometric, electronic and spectroscopic criteria.

S_1 State Low-Valent Models

Low-valent S_1 state models were built using the same protonation patterns as in the S_2L models. The average oxidation state of 3.0 for the S_1 state in the LV scheme can be formed either with all Mn ions as Mn(III), or with the oxidation state pattern II-III₂-IV. The latter is certainly possible, since Mn(IV) and Mn(II) ions are known to coexist without comproportionation.¹⁸²⁻¹⁸⁴ Several S_1L structures were found for which the variational energy minimization leads to the second combination of oxidation states, with the Mn(II) ion always at the Mn4 site (Figure 9). However, this oxidation state

distribution is always energetically disfavored. Among the four-proton models the lowest energy structure S_1L-1 is of the Mn(III)₄ type, whereas the mixed-valent isomers lie at least 17 kcal mol⁻¹ higher in energy. In the set of five-proton models, energy differences between III₄ and II-III₂-IV are smaller, but the two Mn(III)₄ models S_1L-6 and S_1L-7a are still energetically preferred. In all S_1L models the proton of His337 has been transferred to the O3 bridge, as observed in other studies of low oxidation state OEC models.⁹⁰ We note that S_1L-6 corresponds to the model proposed by Pace and Stranger as a best fit to the 1.9 Å resolution crystallographic model.¹⁰⁷ Previously, the same groups had suggested LV S_1 state models corresponding to the present S_1L-1 and S_1L-4 in terms of protonation states and oxidation state distributions.¹⁰⁸

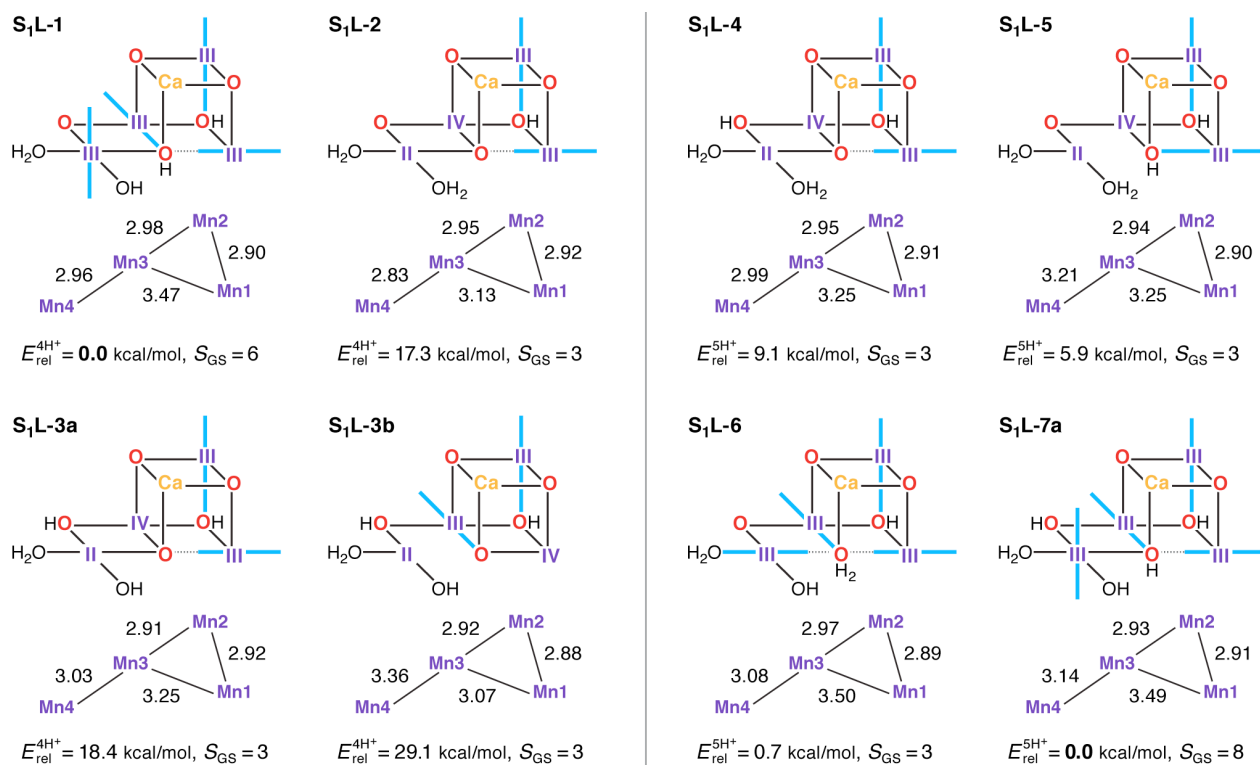


Figure 9. Protonation patterns, oxidation states, Mn–Mn distances (Å), relative total energies (kcal mol⁻¹), and ground spin states for the S_1L models. Blue bars indicate the orientation of Jahn–Teller axes.

In terms of geometry, the results in Figure 9 suggest that regardless of relative energetics, all S_1L models are inconsistent with the EXAFS constraints described previously and with the Mn–Mn distances of the recent XFEL structure.¹¹⁴ Rather than having three or even two short Mn–Mn distances, only one model (S_1L-2) contains a single Mn–Mn distance close to 2.8 Å. Overestimation of these distances by more than 0.1 Å in the DFT models is unlikely since comparison with crystallographic data on Mn(III) complexes confirms that the Mn–O bond lengths, the extent of Jahn–Teller distortions, and the preferred orientation of the Jahn–Teller axes with respect to the nature of the ligands (e.g. O²⁻ vs. OH⁻) are correctly predicted.¹⁸⁵

In terms of electronic structure, no ground state with $S < 3$ is observed for any of the S_1L models, owing to their magnetic

coupling topology: the J_{23} pathway is always ferromagnetic (Table S6) as in the S_1H models and in agreement with experimental and computational data on mixed-valence oxo-bridged model complexes.^{185, 186} However, in contrast to the S_1H models, all S_1L models also display ferromagnetic J_{12} values as a result of O3 protonation, leading to high-spin ground states. The presence or absence of an antiferromagnetic J_{34} interaction differentiates models with $S = 3$ from those with $S = 6$ or $S = 8$ ground states, but the experimentally observed lower spin states ($S = 0$ ground state; low lying $S = 1$ excited state) remain inaccessible for all S_1L models (Fig. 9, Table S9).

S₀ State Low-Valent Models

We also evaluated several models for the S₀ state, all of which display Mn(II)Mn(III)₃ oxidation states (see Figure S12). All S₀L models are at odds with EXAFS Mn–Mn distances for the S₀ state, as the shortest Mn–Mn distance observed is 2.90 Å, whereas the experimental constraints require two or three Mn–Mn distances shorter than 2.80 Å (Table 1). In addition, none of these models reproduces the correct S = 1/2 ground state, yielding instead energetically well-separated high-spin ground states of S = 7/2 or 9/2 (see Table S10). The necessary presence of a Mn(II) ion is also incompatible with the interpretation of ⁵⁵Mn-ENDOR spectra of the S₀ state.^{31, 161, 177}

Mn K pre-edge X-ray absorption spectroscopy

In the preceding sections, EXAFS metrics were used to evaluate the models on a geometric basis. However, complementary information can be derived from the XANES region, which provides insight into the electronic structure. Since the proposed S state models should be consistent with both spectral regions, here we extend the evaluation of the high-valent and low-valent schemes by comparing the Mn K pre-edge XAS spectra of selected structural models with experimental data.²⁴ This serves as an independent control of the electronic structure of these models.

Mn K-edge X-ray absorption spectra arise from excitations of Mn 1s electrons into unoccupied molecular orbitals. These spectra are dominated by dipole-allowed—and thus intense—transitions into Mn 4p orbitals, known as the edge, which can in principle be correlated with the oxidation state of the Mn ions. At lower energies, excitations into unoccupied Mn 3d orbitals are observed; these are formally dipole-forbidden but gain intensity through admixture of 4p character. This defines the pre-edge region that extends over approximately 7 eV and contains information about the local electronic structure and ligand environment of the Mn ions. Computational studies of the Mn K edge (1s–4p) for diverse OEC models have been interpreted in favor of both the LV¹⁰⁶ and the HV¹⁸⁷ schemes, albeit using different theoretical approaches. Given the ambiguities in calculating the Mn K edge, we here focus on the more well-defined and computationally accessible 1s–3d transitions that give rise to the pre-edge spectral region. Importantly, it has been shown that the energies and intensities of calculated pre-edge spectra can be reliably correlated with experiment,^{149, 188–196} using as reference a large set of 17 Mn complexes^{149, 190, 197, 198} with oxidation states ranging from II to V that encompass both the HV and the LV scheme.

The experimental Mn K pre-edge spectra²⁴ of all catalytic intermediates of the OEC are displayed in Figure 10 (top). These are normalized experimental data, where the background of the rising edge has not been subtracted. The pre-edge region extends from 6538–6545 eV, with two features for each intermediate at ca. 6541 eV and 6543 eV. A third, lowest-energy feature is potentially present for S₀ and S₁ at ca. 6539.5 eV. Importantly, the pre-edge peak positions do not move significantly upon oxidation of the cluster. The pre-edge

intensity increases as the cluster advances in the catalytic cycle, with a more pronounced intensity increase between S₀ and S₁ than in the subsequent steps. It should be noted that the subtraction of the rising edge background may alter this visual impression as far as the relative intensities are concerned, but the position of the peak maxima should be largely unaffected by background subtraction.

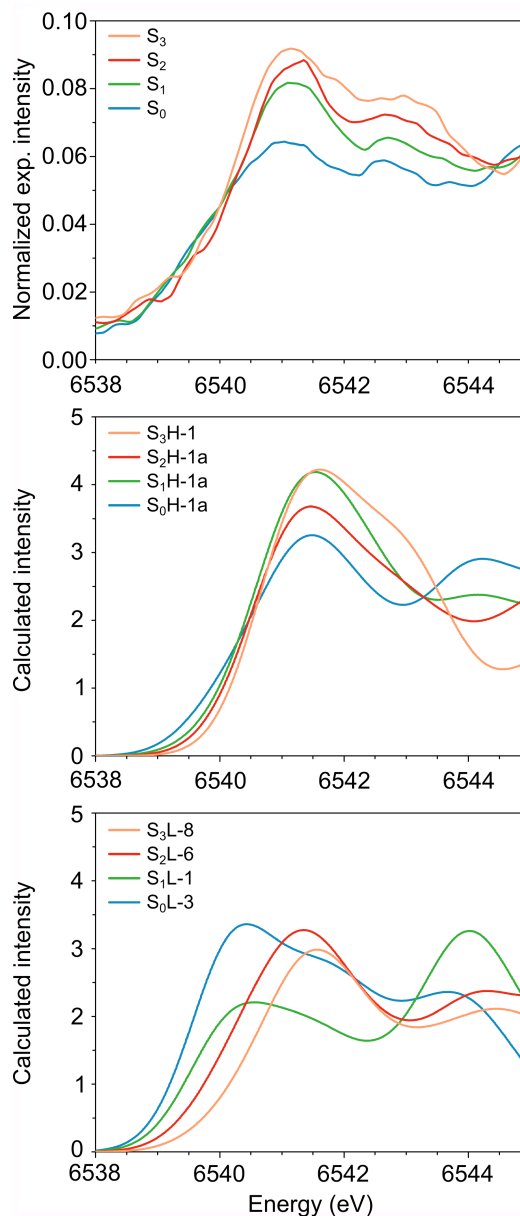


Figure 10. Mn K pre-edge spectra of the OEC. Top to bottom: experimental spectra from Ref. ²⁴, calculated spectra for HV and for LV models. The spectra are colored in blue for S₀, green for S₁, red for S₂ and orange for S₃.

Figure 10 compares the experimental data (top panel) with the calculated pre-edge regions for the best HV (S₀H-1a, S₁H-1a, S₂H-1a, S₃H-1) and LV models (S₀L-3, S₁L-1, S₂L-6, S₃L-8). These calculations do not include the rising edge background, which may affect the relative intensities of the pre-edge spectra. Strikingly, neither the intensity nor the energy

trends are reproduced by the calculated pre-edge spectra of the LV models. The maxima of the first peaks are spread over a range of 1.1 eV, while the spectrum of S_0L-3 is the most intense, both in complete contrast to experiment.

On the other hand, even though there is no perfect agreement in the relative intensities of the S_1 and S_2 state spectra, the peak maxima for all HV models fall within 0.1 eV and thus are in excellent agreement with the experimental data. Quantitative comparison between the calculated and experimental intensities would require fits to experimental data and exceeds the scope of the present work. Analysis of the acceptor orbitals for the lowest energy transitions reveals that the character of the transitions is the same for all models studied here: the excitations are into orbitals of predominant Mn d character with contributions from the directly coordinating ligands. The differences in energy and intensity of the transitions arise from differences in the local ligand sphere symmetries and oxidation states of the Mn ions, and are thus direct probes of their geometric and electronic structures (see the SI for a more detailed discussion of calculated intensities, including a comparison between the pre-edge spectra for the two forms of the S_2 state). Overall, the computed Mn K pre-edge results are in line with the preceding observations: the pre-edge region of the HV models is in agreement with experimental data, while the LV models diverge strongly from experiment for the lowest S states.

CONCLUSIONS

The results presented in this work for all the (semi)stable S states of the OEC, serve to unify diverse experimental observations within a common framework, allowing a definitive conclusion regarding the individual oxidation state assignments for the Mn ions to be reached. We have studied the largest number of low-valent models ever constructed and reported, for all S states, including all known literature suggestions^{107, 108} that can be accommodated within the crystal structure of PSII by Umena et al.¹¹⁰ and expanding considerably beyond them. No variation of protonation level, pattern or bonding topology of structures that follow the low-valent paradigm could produce a consistent set of models for all S_0 – S_3 states. Although individual LV models of the S_2 and S_3 states satisfy some, but never all, experimental criteria, all low-valent S_1 and S_0 state models are in complete disagreement with experiment in all respects. They exhibit too long Mn–Mn distances compared with EXAFS despite the applied backbone constraints, they yield without exception high-spin ground states incompatible with available EPR data, and they have Mn K pre-edge profiles that deviate strongly from experiment. Although the low oxidation state scheme can thus be excluded from further consideration as a valid description of the Kok cycle, the set of LV structures can serve as models of reduced (negative) S states. These can be produced by various treatments^{199–201} and have been invoked as structural models for the photoreduced crystallographic model of the OEC.⁹⁰ Moreover, if sufficiently understood they could provide

important information on the final stages of assembly and activation of the catalytic cluster. A preliminary discussion of the present LV models as candidates for the S_{-1} and S_{-2} states of the OEC is provided in the SI.

In contrast, using models constructed according to the high-valent paradigm leads to excellent agreement with experimental constraints for the individual intermediates. Importantly a self-consistent progression of states, comprising structures which served as the best models for individual S states, is observed. This model set is simultaneously consistent with experimental constraints concerning deprotonation and water-binding events along the catalytic cycle (see Figure 11). With respect to questions relevant to the HV scheme itself, specifically the precise identity and distribution of Mn oxidation states in the S_0 state and the possibility of ligand radical formation in the S_3 state,^{23–27, 61, 64, 66} the present work supports the absence of Mn(II) in the S_0 state and the Mn-centered oxidation in the S_2 – S_3 transition.

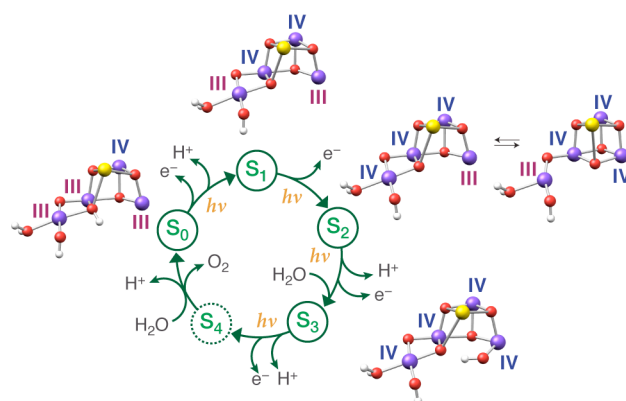


Figure 11. Models for each S state of the Kok cycle, showing the optimized geometry, protonation pattern and Mn oxidation states of the inorganic core.

Although no similar comprehensive comparison of the two oxidation state paradigms has been attempted before, we note that in addition to the agreement with EXAFS distances, support for the HV scheme derives from simulations of EXAFS spectra for individual high-valent models, some of which resemble closely the ones selected here as best HV candidates.^{78, 80, 202} It is also important to stress that despite hypothetical water oxidation mechanisms that might be accommodated within an LV scheme, to the best of our knowledge it is only with high-valent models that complete and detailed mechanistic pathways for water oxidation have been proposed from quantum chemical calculations.^{67–70, 73} As reported also for synthetic Mn systems,²⁰³ the high oxidation states of the Mn ions are presumably related to oxyl radical formation.^{204, 205} This is the basis of the most prevalent mechanistic hypothesis proposed by Siegbahn on the basis of energy optimization, where O–O bond formation is proposed to advance through low-barrier oxo–oxyl coupling in the S_4 state.^{69, 73, 206} Note that the assignment of high oxidation states for the Mn ions for the biological OEC is also in agreement with the assignment of average Mn oxidation states close to

Mn(IV) for synthetic manganese oxide water oxidation catalysts.²⁰⁷

In summary, it was shown through extensive comparison of high-valent and low-valent models for the individual S₀–S₃ state catalytic intermediates of the OEC that only the high-valent scheme, that is, Mn(III)₃Mn(IV) for the S₀ state up to Mn(IV)₄ for the S₃ state, can lead to spectroscopically consistent models for all (semi)stable catalytic intermediates. Further advances in our understanding of the dynamic structure and the regulation of the OEC in these states remain necessary and are currently being pursued by many research groups. One of the greatest challenges now appears to lie in obtaining experimental information about the most critical final steps of water oxidation, that is, on the transient states related to oxygen evolution and regeneration of the S₀ state. It is expected that information obtained by new techniques such as X-ray free-electron laser protein crystallography,^{114, 208, 209} coupled with high-level spectroscopy-oriented quantum chemical approaches, will be pivotal for achieving this goal in the near future.

Acknowledgements

Alain Boussac is gratefully acknowledged for providing the EPR samples. Financial support was provided by the Max Planck Society. JM was supported by Energimyndigheten, the Solar Fuels strong research environment (Umeå University) and the Artificial Leaf Project Umeå (K&A Wallenberg foundation).

Notes and references

^a Max Planck Institute for Chemical Energy Conversion, Stiftstr. 34-38, 45470 Mülheim an der Ruhr, Germany.

^b Department of Chemistry, Chemical Biological Center (KBC), Umeå University, 90187 Umeå, Sweden.

Electronic Supplementary Information (ESI) available: Additional methodological details and discussion, Tables S1–S10, Figures S1–S16, spin populations, parameters of optimized structures, experimental details and analysis of ⁵⁵Mn ENDOR at 2.5 K, analysis of calculated Mn K pre-edge XAS, discussion of reduced S states. See DOI: 10.1039/b000000x/

1. T. A. Faunce, W. Lubitz, A. W. Rutherford, D. MacFarlane, G. F. Moore, P. Yang, D. G. Nocera, T. A. Moore, D. H. Gregory, S. Fukuzumi, K. B. Yoon, F. A. Armstrong, M. R. Wasielewski and S. Styring, *Energy Environ. Sci.*, 2013, **6**, 695-698.
2. T. R. Cook, D. K. Dogutan, S. Y. Reece, Y. Surendranath, T. S. Teets and D. G. Nocera, *Chem. Rev.*, 2010, **110**, 6474-6502.
3. W. Lubitz, E. J. Reijerse and J. Messinger, *Energy Environ. Sci.*, 2008, **1**, 15-31.
4. M. D. Kärkäs, O. Verho, E. V. Johnston and B. Åkermark, *Chem. Rev.*, 2014.
5. S. Berardi, S. Drouet, L. Francas, C. Gimbert-Surinach, M. Guttentag, C. Richmond, T. Stoll and A. Llobet, *Chem. Soc. Rev.*, 2014, **43**, 7501-7519.
6. D. G. Nocera, *Acc. Chem. Res.*, 2012, **45**, 767-776.
7. M. Wiechen, H.-M. Berends and P. Kurz, *Dalton Trans.*, 2012, **41**, 21-31.
8. J. P. McEvoy and G. W. Brudvig, *Chem. Rev.*, 2006, **106**, 4455-4483.
9. N. Cox, D. A. Pantazis, F. Neese and W. Lubitz, *Acc. Chem. Res.*, 2013, **46**, 1588-1596.
10. J. Messinger and G. Renger, in *Primary Processes of Photosynthesis, Part 2: Principles and Apparatus*, The Royal Society of Chemistry, Cambridge, 2008, vol. 9, pp. 291-349.
11. A. Grundmeier and H. Dau, *Biochim. Biophys. Acta Bioenerg.*, 2012, **1817**, 88-105.
12. D. A. Pantazis, N. Cox, W. Lubitz and F. Neese, in *Encyclopedia of Inorganic and Bioinorganic Chemistry*, John Wiley & Sons, Ltd, 2014.
13. P. Joliot, G. Barbieri and R. Chabaud, *Photochem. Photobiol.*, 1969, **10**, 309-329.
14. B. Kok, B. Forbush and M. McGloin, *Photochem. Photobiol.*, 1970, **11**, 457-475.
15. D. J. Vinyard, G. M. Ananyev and G. C. Dismukes, *Annu. Rev. Biochem.*, 2013, **82**, 577-606.
16. G. C. Dismukes and Y. Siderer, *Proc. Natl. Acad. Sci. USA*, 1981, **78**, 274-278.
17. D. B. Goodin, V. K. Yachandra, R. D. Britt, K. Sauer and M. P. Klein, *Biochim. Biophys. Acta Bioenerg.*, 1984, **767**, 209-216.
18. J. C. de Paula, W. F. Beck, A.-F. Miller, R. B. Wilson and G. W. Brudvig, *J. Chem. Soc., Faraday Trans.*, 1987, **83**, 3635-3651.
19. J. C. De Paula and G. W. Brudvig, *J. Am. Chem. Soc.*, 1985, **107**, 2643-2648.
20. J. C. De Paula, W. F. Beck and G. W. Brudvig, *J. Am. Chem. Soc.*, 1986, **108**, 4002-4009.
21. G. W. Brudvig, W. F. Beck and J. C. de Paula, *Annu. Rev. Biophys. Biophys. Chem.*, 1989, **18**, 25-46.
22. O. Hansson and L. E. Andreasson, *Biochim. Biophys. Acta*, 1982, **679**, 261-268.
23. H. Dau, L. Iuzzolino and J. Dittmer, *Biochim. Biophys. Acta Bioenerg.*, 2001, **1503**, 24-39.
24. J. Messinger, J. H. Robblee, U. Bergmann, C. Fernandez, P. Glatzel, H. Visser, R. M. Cinco, K. L. McFarlane, E. Bellacchio, S. A. Pizarro, S. P. Cramer, K. Sauer, M. P. Klein and V. K. Yachandra, *J. Am. Chem. Soc.*, 2001, **123**, 7804-7820.
25. T.-a. Ono, T. Noguchi, Y. Inoue, M. Kusunoki, T. Matsushita and H. Oyanagi, *Science*, 1992, **258**, 1335-1337.
26. L. Iuzzolino, J. Dittmer, W. Dörner, W. Meyer-Klaucke and H. Dau, *Biochemistry*, 1998, **37**, 17112-17119.
27. T. A. Roelofs, W. Liang, M. J. Latimer, R. M. Cinco, A. Rompel, J. C. Andrews, K. Sauer, V. K. Yachandra and M. P. Klein, *Proc. Natl. Acad. Sci. U.S.A.*, 1996, **93**, 3335-3340.
28. R. J. Pace, L. Jin and R. Stranger, *Dalton Trans.*, 2012, **41**, 11145-11160.
29. M. Zheng and G. C. Dismukes, *Inorg. Chem.*, 1996, **35**, 3307-3319.
30. L. Jin, P. Smith, C. J. Noble, R. Stranger, G. R. Hanson and R. J. Pace, *Phys. Chem. Chem. Phys.*, 2014, **16**, 7799-7812.
31. L. V. Kulik, B. Epel, W. Lubitz and J. Messinger, *J. Am. Chem. Soc.*, 2007, **129**, 13421-13435.
32. J. M. Peloquin, K. A. Campbell, D. W. Randall, M. A. Evanchik, V. L. Pecoraro, W. H. Armstrong and R. D. Britt, *J. Am. Chem. Soc.*, 2000, **122**, 10926-10942.

33. J. M. Peloquin and R. D. Britt, *Biochim. Biophys. Acta Bioenerg.*, 2001, **1503**, 96-111.
34. N. Ioannidis, G. Zahariou and V. Petrouleas, *Biochemistry*, 2006, **45**, 6252-6259.
35. A. Haddy, *Photosynth. Res.*, 2007, **92**, 357-368.
36. K. A. Åhring, S. Peterson and S. Styring, *Biochemistry*, 1997, **36**, 13148-13152.
37. J. Messinger, J. H. A. Nugent and M. C. W. Evans, *Biochemistry*, 1997, **36**, 11055-11060.
38. J. Messinger, J. H. Robblee, W. O. Yu, K. Sauer, V. K. Yachandra and M. P. Klein, *J. Am. Chem. Soc.*, 1997, **119**, 11349-11350.
39. K. A. Åhring, S. Peterson and S. Styring, *Biochemistry*, 1998, **37**, 8115-8120.
40. D. Koulougliotis, D. J. Hirsh and G. W. Brudvig, *J. Am. Chem. Soc.*, 1992, **114**, 8322-8323.
41. W.-Y. Hsieh, K. A. Campbell, W. Gregor, R. D. Britt, D. W. Yoder, J. E. Penner-Hahn and V. L. Pecoraro, *Biochim. Biophys. Acta Bioenerg.*, 2004, **1655**, 149-157.
42. J. L. Zimmermann and A. W. Rutherford, *Biochemistry*, 1986, **25**, 4609-4615.
43. A. Haddy, K. V. Lakshmi, G. W. Brudvig and H. A. Frank, *Biophys. J.*, 2004, **87**, 2885-2896.
44. N. Ioannidis and V. Petrouleas, *Biochemistry*, 2000, **39**, 5246-5254.
45. A. Boussac, M. Sugiura, A. W. Rutherford and P. Dorlet, *J. Am. Chem. Soc.*, 2009, **131**, 5050-5051.
46. N. Cox, M. Retegan, F. Neese, D. A. Pantazis, A. Boussac and W. Lubitz, *Science*, 2014, **345**, 804-808.
47. L. Zaltsman, G. M. Ananyev, E. Bruntrager and G. C. Dismukes, *Biochemistry*, 1997, **36**, 8914-8922.
48. J. Dasgupta, G. M. Ananyev and G. C. Dismukes, *Coord. Chem. Rev.*, 2008, **252**, 347-360.
49. D. R. J. Kolling, N. Cox, G. M. Ananyev, R. J. Pace and G. C. Dismukes, *Biophys. J.*, 2012, **103**, 313-322.
50. T. Kuntzleman and C. F. Yocum, *Biochemistry*, 2005, **44**, 2129-2142.
51. J. Messinger, G. Seaton, T. Wydrzynski, U. Wacker and G. Renger, *Biochemistry*, 1997, **36**, 6862-6873.
52. J. Messinger, M. Badger and T. Wydrzynski, *Proc. Natl. Acad. Sci. U. S. A.*, 1995, **92**, 3209-3213.
53. K. Beckmann, J. Messinger, M. Badger, T. Wydrzynski and W. Hillier, *Photosynth. Res.*, 2009, **102**, 511-522.
54. N. Cox and J. Messinger, *Biochim. Biophys. Acta Bioenerg.*, 2013, **1827**, 1020-1030.
55. W. Hillier and T. Wydrzynski, *Biochim. Biophys. Acta Bioenerg.*, 2001, **1503**, 197-209.
56. J. Messinger, *Phys. Chem. Chem. Phys.*, 2004, **6**, 4764-4771.
57. W. Hillier and T. Wydrzynski, *Coord. Chem. Rev.*, 2008, **252**, 306-317.
58. J. Cole, V. K. Yachandra, R. D. Guiles, A. E. McDermott, R. D. Britt, S. L. Dexheimer, K. Sauer and M. P. Klein, *Biochim. Biophys. Acta Bioenerg.*, 1987, **890**, 395-398.
59. V. K. Yachandra, K. Sauer and M. P. Klein, *Chem. Rev.*, 1996, **96**, 2927-2950.
60. V. K. Yachandra, V. J. DeRose, M. J. Latimer, I. Mukerji, K. Sauer and M. P. Klein, *Science*, 1993, **260**, 675-679.
61. H. Dau, P. Liebisch and M. Haumann, *Anal. Bioanal. Chem.*, 2003, **376**, 562-583.
62. M. Haumann, C. Müller, P. Liebisch, L. Iuzzolino, J. Dittmer, M. Grabolle, T. Neisius, W. Meyer-Klaucke and H. Dau, *Biochemistry*, 2005, **44**, 1894-1908.
63. D. Kuzek and R. J. Pace, *Biochim. Biophys. Acta Bioenerg.*, 2001, **1503**, 123-137.
64. R. D. Guiles, J. L. Zimmermann, A. E. McDermott, V. K. Yachandra, J. L. Cole, S. L. Dexheimer, R. D. Britt, K. Wieghardt and U. Bossek, *Biochemistry*, 1990, **29**, 471-485.
65. D. J. MacLachlan, J. H. A. Nugent and M. C. W. Evans, *Biochim. Biophys. Acta Bioenerg.*, 1994, **1185**, 103-111.
66. H. Dau, P. Liebisch and M. Haumann, *Phys. Scr.*, 2005, **2005**, 844.
67. P. E. M. Siegbahn, *Chem.—Eur. J.*, 2008, **14**, 8290-8302.
68. P. E. M. Siegbahn, *Phil. Trans. R. Soc. B*, 2008, **363**, 1221-1228.
69. P. E. M. Siegbahn, *Acc. Chem. Res.*, 2009, **42**, 1871-1880.
70. P. E. M. Siegbahn, *J. Photochem. Photobiol., B*, 2011, **104**, 94-99.
71. P. E. M. Siegbahn, *Phys. Chem. Chem. Phys.*, 2012, **14**, 4849-4856.
72. P. E. M. Siegbahn, *J. Am. Chem. Soc.*, 2013, **135**, 9442-9449.
73. P. E. M. Siegbahn, *Biochim. Biophys. Acta Bioenerg.*, 2013, **1827**, 1003-1019.
74. E. M. Sproviero, J. A. Gascon, J. P. McEvoy, G. W. Brudvig and V. S. Batista, *J. Chem. Theory Comput.*, 2006, **2**, 1119-1134.
75. E. M. Sproviero, J. A. Gascon, J. P. McEvoy, G. W. Brudvig and V. S. Batista, *J. Am. Chem. Soc.*, 2008, **130**, 6728-6730.
76. E. M. Sproviero, J. A. Gascon, J. P. McEvoy, G. W. Brudvig and V. S. Batista, *J. Am. Chem. Soc.*, 2008, **130**, 3428-3442.
77. E. M. Sproviero, J. A. Gascon, J. P. McEvoy, G. W. Brudvig and V. S. Batista, *Coord. Chem. Rev.*, 2008, **252**, 395-415.
78. S. Lubber, I. Rivalta, Y. Umena, K. Kawakami, J. R. Shen, N. Kamiya, G. W. Brudvig and V. S. Batista, *Biochemistry*, 2011, **50**, 6308-6311.
79. I. Rivalta, M. Amin, S. Lubber, S. Vassiliev, R. Pokhrel, Y. Umena, K. Kawakami, J. R. Shen, N. Kamiya, D. Bruce, G. W. Brudvig, M. R. Gunner and V. S. Batista, *Biochemistry*, 2011, **50**, 6312-6315.
80. R. Pal, C. F. A. Negre, L. Vogt, R. Pokhrel, M. Z. Ertem, G. W. Brudvig and V. S. Batista, *Biochemistry*, 2013, **52**, 7703-7706.
81. K. Kanda, S. Yamanaka, T. Saito, Y. Umena, K. Kawakami, J.-R. Shen, N. Kamiya, M. Okumura, H. Nakamura and K. Yamaguchi, *Chem. Phys. Lett.*, 2011, **506**, 98-103.
82. H. Isobe, M. Shoji, S. Yamanaka, Y. Umena, K. Kawakami, N. Kamiya, J. R. Shen and K. Yamaguchi, *Dalton Trans.*, 2012, **41**, 13727-13740.
83. T. Saito, S. Yamanaka, K. Kanda, H. Isobe, Y. Takano, Y. Shigeta, Y. Umena, K. Kawakami, J. R. Shen, N. Kamiya, M. Okumura, M. Shoji, Y. Yoshioka and K. Yamaguchi, *Int. J. Quantum Chem.*, 2012, **112**, 253-276.
84. K. Yamaguchi, H. Isobe, S. Yamanaka, T. Saito, K. Kanda, M. Shoji, Y. Umena, K. Kawakami, J. R. Shen, N. Kamiya and M. Okumura, *Int. J. Quantum Chem.*, 2012, **113**, 525-541.
85. S. Yamanaka, T. Saito, K. Kanda, H. Isobe, Y. Umena, K. Kawakami, J. R. Shen, N. Kamiya, M. Okumura, H. Nakamura and K. Yamaguchi, *Int. J. Quantum Chem.*, 2012, **112**, 321-343.
86. M. Shoji, H. Isobe, S. Yamanaka, Y. Umena, K. Kawakami, N. Kamiya, J. R. Shen and K. Yamaguchi, *Catal. Sci. Technol.*, 2013, **3**, 1831-1848.
87. K. Yamaguchi, S. Yamanaka, H. Isobe, T. Saito, K. Kanda, Y. Umena, K. Kawakami, J. R. Shen, N. Kamiya, M. Okumura, H.

- Nakamura, M. Shoji and Y. Yoshioka, *Int. J. Quantum Chem.*, 2013, **113**, 453-473.
88. M. Kusunoki, *Biochim. Biophys. Acta Bioenerg.*, 2007, **1767**, 484-492.
89. M. Kusunoki, *Photochem. Photobiol. B*, 2011, **104**, 100-110.
90. A. Galstyan, A. Robertazzi and E. W. Knapp, *J. Am. Chem. Soc.*, 2012, **134**, 7442-7449.
91. D. Bovi, D. Narzi and L. Guidoni, *Angew. Chem., Int. Ed.*, 2013, **52**, 11744-11749.
92. S. Schinzel, J. Schraut, A. V. Arbuznikov, P. E. M. Siegbahn and M. Kaupp, *Chem.—Eur. J.*, 2010, **16**, 10424-10438.
93. D. A. Pantazis, M. Orio, T. Petrenko, S. Zein, W. Lubitz, J. Messinger and F. Neese, *Phys. Chem. Chem. Phys.*, 2009, **11**, 6788-6798.
94. W. Ames, D. A. Pantazis, V. Krewald, N. Cox, J. Messinger, W. Lubitz and F. Neese, *J. Am. Chem. Soc.*, 2011, **133**, 19743-19757.
95. N. Cox, L. Rapatskiy, J.-H. Su, D. A. Pantazis, M. Sugiura, L. Kulik, P. Dorlet, A. W. Rutherford, F. Neese, A. Boussac, W. Lubitz and J. Messinger, *J. Am. Chem. Soc.*, 2011, **133**, 3635-3648.
96. J.-H. Su, N. Cox, W. Ames, D. A. Pantazis, L. Rapatskiy, T. Lohmiller, L. V. Kulik, P. Dorlet, A. W. Rutherford, F. Neese, A. Boussac, W. Lubitz and J. Messinger, *Biochim. Biophys. Acta Bioenerg.*, 2011, **1807**, 829-840.
97. D. A. Pantazis, W. Ames, N. Cox, W. Lubitz and F. Neese, *Angew. Chem., Int. Ed.*, 2012, **51**, 9935-9940.
98. M. Pérez Navarro, W. M. Ames, H. Nilsson, T. Lohmiller, D. A. Pantazis, L. Rapatskiy, M. M. Nowaczyk, F. Neese, A. Boussac, J. Messinger, W. Lubitz and N. Cox, *Proc. Natl. Acad. Sci. U.S.A.*, 2013, **110**, 15561-15566.
99. M. Retegan, F. Neese and D. A. Pantazis, *J. Chem. Theory Comput.*, 2013, **9**, 3832-3842.
100. T. Lohmiller, V. Krewald, M. Pérez Navarro, M. Retegan, L. Rapatskiy, M. M. Nowaczyk, A. Boussac, F. Neese, W. Lubitz, D. A. Pantazis and N. Cox, *Phys. Chem. Chem. Phys.*, 2014, **16**, 11877-11892.
101. Y. Kurashige, G. K.-L. Chan and T. Yanai, *Nat Chem*, 2013, **5**, 660-666.
102. M. Retegan, N. Cox, W. Lubitz, F. Neese and D. A. Pantazis, *Phys. Chem. Chem. Phys.*, 2014, **16**, 11901-11910.
103. D. Narzi, D. Bovi and L. Guidoni, *Proc. Natl. Acad. Sci. U.S.A.*, 2014, **111**, 8723-8728.
104. S. Petrie, R. Stranger, P. Gatt and R. J. Pace, *Chem.—Eur. J.*, 2007, **13**, 5082-5089.
105. S. Petrie, R. Stranger and R. L. Pace, *Chem.—Eur. J.*, 2008, **14**, 5482-5494.
106. A. R. Jaszewski, S. Petrie, R. J. Pace and R. Stranger, *Chem.—Eur. J.*, 2011, **17**, 5699-5713.
107. P. Gatt, S. Petrie, R. Stranger and R. J. Pace, *Angew. Chem., Int. Ed.*, 2012, **51**, 12025-12028.
108. S. Petrie, P. Gatt, R. Stranger and R. J. Pace, *Phys. Chem. Chem. Phys.*, 2012, **14**, 11333-11343.
109. A. R. Jaszewski, R. Stranger and R. J. Pace, *J. Phys. Chem. B*, 2011, **115**, 4484-4499.
110. Y. Umena, K. Kawakami, J.-R. Shen and N. Kamiya, *Nature*, 2011, **473**, 55-60.
111. J. Yano, J. Kern, K.-D. Irrgang, M. J. Latimer, U. Bergmann, P. Glatzel, Y. Pushkar, J. Biesiadka, B. Loll, K. Sauer, J. Messinger, A. Zouni and V. K. Yachandra, *Proc. Natl. Acad. Sci. USA*, 2005, **102**, 12047-12052.
112. M. Grabolle, M. Haumann, C. Müller, P. Liebisch and H. Dau, *J. Biol. Chem.*, 2006, **281**, 4580-4588.
113. A. Robertazzi, A. Galstyan and E. W. Knapp, *CrystEngComm*, 2011, **13**, 6369-6372.
114. M. Suga, F. Akita, K. Hirata, G. Ueno, H. Murakami, Y. Nakajima, T. Shimizu, K. Yamashita, M. Yamamoto, H. Ago and J.-R. Shen, *Nature*, 2014, DOI: 10.1038/nature13991.
115. J. Yano and V. Yachandra, *Chem. Rev.*, 2014, **114**, 4175-4205.
116. H. Dau, A. Grundmeier, P. Loja and M. Haumann, *Phil. Trans. R. Soc. B*, 2008, **363**, 1237-1243.
117. J. Yano, J. Kern, K. Sauer, M. J. Latimer, Y. Pushkar, J. Biesiadka, B. Loll, W. Saenger, J. Messinger, A. Zouni and V. K. Yachandra, *Science*, 2006, **314**, 821-825.
118. Y. Pushkar, J. Yano, P. Glatzel, J. Messinger, A. Lewis, K. Sauer, U. Bergmann and V. Yachandra, *J. Biol. Chem.*, 2007, **282**, 7198-7208.
119. J. Yano, Y. Pushkar, P. Glatzel, A. Lewis, K. Sauer, J. Messinger, U. Bergmann and V. Yachandra, *J. Am. Chem. Soc.*, 2005, **127**, 14974-14975.
120. C. Glöckner, J. Kern, M. Broser, A. Zouni, V. Yachandra and J. Yano, *J. Biol. Chem.*, 2013, **288**, 22607-22620.
121. W. Liang, T. A. Roelofs, R. M. Cinco, A. Rompel, M. J. Latimer, W. O. Yu, K. Sauer, M. P. Klein and V. K. Yachandra, *J. Am. Chem. Soc.*, 2000, **122**, 3399-3412.
122. D. A. Pantazis, M. Orio, T. Petrenko, S. Zein, E. Bill, W. Lubitz, J. Messinger and F. Neese, *Chem.—Eur. J.*, 2009, **15**, 5108-5123.
123. C. Baffert, M. Orio, D. A. Pantazis, C. Duboc, A. G. Blackman, G. Blondin, F. Neese, A. Deronzier and M.-N. Collomb, *Inorg. Chem.*, 2009, **48**, 10281-10288.
124. M. Orio, D. A. Pantazis, T. Petrenko and F. Neese, *Inorg. Chem.*, 2009, **48**, 7251-7260.
125. S. Schinzel and M. Kaupp, *Can. J. Chem.*, 2009, **87**, 1521-1539.
126. J. Schraut, A. V. Arbuznikov, S. Schinzel and M. Kaupp, *ChemPhysChem*, 2011, **12**, 3170-3179.
127. V. Krewald, F. Neese and D. A. Pantazis, *J. Am. Chem. Soc.*, 2013, **135**, 5726-5739.
128. J. H. Robblee, J. Messinger, R. M. Cinco, K. L. McFarlane, C. Fernandez, S. A. Pizarro, K. Sauer and V. K. Yachandra, *J. Am. Chem. Soc.*, 2002, **124**, 7459-7471.
129. H. Dau and M. Haumann, *Coord. Chem. Rev.*, 2008, **252**, 273-295.
130. R. M. Cinco, J. H. Robblee, A. Rompel, C. Fernandez, V. K. Yachandra, K. Sauer and M. P. Klein, *J. Phys. Chem. B*, 1998, **102**, 8248-8256.
131. R. M. Cinco, K. L. McFarlane Holman, J. H. Robblee, J. Yano, S. A. Pizarro, E. Bellacchio, K. Sauer and V. K. Yachandra, *Biochemistry*, 2002, **41**, 12928-12933.
132. Y. Pushkar, J. Yano, K. Sauer, A. Boussac and V. K. Yachandra, *Proc. Natl. Acad. Sci. U.S.A.*, 2008, **105**, 1879-1884.

133. H. Dau and M. Haumann, *J. Synchrotron Radiat.*, 2003, **10**, 76-85.
134. M.-F. Charlot, A. Boussac and G. Blondin, *Biochim. Biophys. Acta Bioenerg.*, 2005, **1708**, 120-132.
135. F. Neese, *WIREs Comput. Mol. Sci.*, 2012, **2**, 73-78.
136. E. van Lenthe, E. J. Baerends and J. G. Snijders, *J. Chem. Phys.*, 1993, **99**, 4597-4610.
137. E. van Lenthe, E. J. Baerends and J. G. Snijders, *J. Chem. Phys.*, 1994, **101**, 9783-9792.
138. C. van Wüllen, *J. Chem. Phys.*, 1998, **109**, 392-399.
139. M. Filatov and D. Cremer, *Mol. Phys.*, 2003, **101**, 2295-2302.
140. S. Grimme, J. Antony, S. Ehrlich and H. Krieg, *J. Chem. Phys.*, 2010, **132**, 154104-154119.
141. J. P. Perdew, *Phys. Rev. B*, 1986, **33**, 8822-8824.
142. A. D. Becke, *Phys. Rev. A*, 1988, **38**, 3098-3100.
143. D. A. Pantazis, X. Y. Chen, C. R. Landis and F. Neese, *J. Chem. Theory Comput.*, 2008, **4**, 908-919.
144. F. Weigend and R. Ahlrichs, *Phys. Chem. Chem. Phys.*, 2005, **7**, 3297-3305.
145. F. Weigend, *Phys. Chem. Chem. Phys.*, 2006, **8**, 1057-1065.
146. A. Klamt and D. Schürman, *J. Chem. Soc., Perkin Trans. 2*, 1993, 799-805.
147. V. N. Staroverov, G. E. Scuseria, J. Tao and J. P. Perdew, *J. Chem. Phys.*, 2003, **119**, 12129-12137.
148. F. Neese, F. Wennmohs, A. Hansen and U. Becker, *Chem. Phys.*, 2009, **356**, 98-109.
149. M. Roemelt, M. A. Beckwith, C. Duboc, M.-N. Collomb, F. Neese and S. DeBeer, *Inorg. Chem.*, 2012, **51**, 680-687.
150. M. Sugiura, F. Rappaport, K. Brettel, T. Noguchi, A. W. Rutherford and A. Boussac, *Biochemistry*, 2004, **43**, 13549-13563.
151. E. Reijerse, F. Lendzian, R. Isaacson and W. Lubitz, *J. Magn. Reson.*, 2012, **214**, 237-243.
152. A. Schweiger and G. Jeschke, *Principles of pulse electron paramagnetic resonance*, Oxford University Press, Oxford, 2001.
153. U. Bossek, H. Hummel, T. Weyhermüller, K. Wieghardt, S. Russell, L. van der Wolf and U. Kolb, *Angew. Chem., Int. Ed.*, 1996, **35**, 1552-1554.
154. P. E. M. Siegbahn, *ChemPhysChem*, 2011, **12**, 3274-3280.
155. J. Schraut and M. Kaupp, *Chem.—Eur. J.*, 2014, **20**, 7300-7308.
156. A. Robertazzi, A. Galstyan and E. W. Knapp, *Biochim. Biophys. Acta Bioenerg.*, 2014, **1837**, 1316-1321.
157. P. E. M. Siegbahn, *Phys. Chem. Chem. Phys.*, 2014, **16**, 11893-11900.
158. L. Rapatskiy, N. Cox, A. Savitsky, W. M. Ames, J. Sander, M. M. Nowaczyk, M. Rögner, A. Boussac, F. Neese, J. Messinger and W. Lubitz, *J. Am. Chem. Soc.*, 2012, **134**, 16619-16634.
159. C. P. Aznar and R. D. Britt, *Phil. Trans. R. Soc. B*, 2002, **357**, 1359-1366.
160. N. Cox, W. Ames, B. Epel, L. V. Kulik, L. Rapatskiy, F. Neese, J. Messinger, K. Wieghardt and W. Lubitz, *Inorg. Chem.*, 2011, **50**, 8238-8251.
161. L. V. Kulik, B. Epel, W. Lubitz and J. Messinger, *J. Am. Chem. Soc.*, 2005, **127**, 2392-2393.
162. A. Klauss, M. Haumann and H. Dau, *Proc. Natl. Acad. Sci. U.S.A.*, 2012, **109**, 16035-16040.
163. T. Noguchi, *Phil. Trans. R. Soc. B*, 2008, **363**, 1189-1195.
164. H. Suzuki, M. Sugiura and T. Noguchi, *Biochemistry*, 2008, **47**, 11024-11030.
165. H. Nilsson, T. Krupnik, J. Kargul and J. Messinger, *Biochim. Biophys. Acta Bioenerg.*, 2014, **1837**, 1257-1262.
166. P. Glatzel, H. Schroeder, Y. Pushkar, T. Boron, S. Mukherjee, G. Christou, V. L. Pecoraro, J. Messinger, V. K. Yachandra, U. Bergmann and J. Yano, *Inorg. Chem.*, 2013, **52**, 5642-5644.
167. J. L. Zimmermann and A. W. Rutherford, *Biochim. Biophys. Acta Bioenerg.*, 1984, **767**, 160-167.
168. G. W. Brudvig, J. L. Casey and K. Sauer, *Biochim. Biophys. Acta Bioenerg.*, 1983, **723**, 366-371.
169. M. Haumann, O. Bögershausen and W. Junge, *FEBS Lett.*, 1994, **355**, 101-105.
170. M. Haumann, O. Bögershausen, D. Cherepanov, R. Ahlbrink and W. Junge, *Photosynth. Res.*, 1997, **51**, 193-208.
171. W. Hillier and T. Wydrzynski, *Biochemistry*, 2000, **39**, 4399-4405.
172. M. Iizasa, H. Suzuki and T. Noguchi, *Biochemistry*, 2010, **49**, 3074-3082.
173. R. J. Debus, *Coord. Chem. Rev.*, 2008, **252**, 244-258.
174. S. Styring and A. W. Rutherford, *Biochemistry*, 1987, **26**, 2401-2405.
175. S. Styring and A. W. Rutherford, *Biochim. Biophys. Acta Bioenerg.*, 1988, **933**, 378-387.
176. J. H. Robblee, R. M. Cinco and V. K. Yachandra, *Biochim. Biophys. Acta Bioenerg.*, 2001, **1503**, 7-23.
177. L. V. Kulik, W. Lubitz and J. Messinger, *Biochemistry*, 2005, **44**, 9368-9374.
178. T. Ichino and Y. Yoshioka, *Chem. Phys. Lett.*, 2012, **545**, 107-111.
179. M. Lundberg and P. E. M. Siegbahn, *Phys. Chem. Chem. Phys.*, 2004, **6**, 4772-4780.
180. Z. Deák, S. Peterson, P. Geijer, K. A. Åhring and S. Styring, *Biochim. Biophys. Acta Bioenerg.*, 1999, **1412**, 240-249.
181. B. Nöring, D. Shevela, G. Renger and J. Messinger, *Photosynth. Res.*, 2008, **98**, 251-260.
182. T. Afrati, C. Dendrinou-Samara, C. R. Raptoulou, A. Terzis, V. Tangoulis and D. P. Kessissoglou, *Angew. Chem., Int. Ed.*, 2002, **41**, 2148-2150.
183. M. Alexiou, C. Dendrinou-Samara, A. Karagianni, S. Biswas, C. M. Zaleski, J. Kampf, D. Yoder, J. E. Penner-Hahn, V. L. Pecoraro and D. P. Kessissoglou, *Inorg. Chem.*, 2003, **42**, 2185-2187.
184. M. K. Chan and W. H. Armstrong, *J. Am. Chem. Soc.*, 1990, **112**, 4985-4986.
185. T. C. Stamatatos and G. Christou, *Phil. Trans. R. Soc. A*, 2008, **366**, 113-125.
186. D. A. Pantazis, V. Krewald, M. Orto and F. Neese, *Dalton Trans.*, 2010, **39**, 4959-4967.
187. B. Brena, P. E. M. Siegbahn and H. Ågren, *J. Am. Chem. Soc.*, 2012, **134**, 17157-17167.
188. S. DeBeer George, T. Petrenko and F. Neese, *J. Phys. Chem. A*, 2008, **112**, 12936-12943.
189. P. Chandrasekaran, S. C. E. Stieber, T. J. Collins, J. L. Que, F. Neese and S. DeBeer, *Dalton Trans.*, 2011, **40**, 11070-11079.

190. V. Krewald, B. Lassalle-Kaiser, T. T. Boron, C. J. Pollock, J. Kern, M. A. Beckwith, V. K. Yachandra, V. L. Pecoraro, J. Yano, F. Neese and S. DeBeer, *Inorg. Chem.*, 2013, **52**, 12904-12914.
191. F. A. Lima, R. Bjornsson, T. Weyhermuller, P. Chandrasekaran, P. Glatzel, F. Neese and S. DeBeer, *Phys. Chem. Chem. Phys.*, 2013, **15**, 20911-20920.
192. D. F. Leto and T. A. Jackson, *Inorg. Chem.*, 2014, **53**, 6179-6194.
193. N. Leidel, P. Chernev, K. G. V. Havelius, S. Ezzaher, S. Ott and M. Haumann, *Inorg. Chem.*, 2012, **51**, 4546-4559.
194. T. J. Penfold, S. Karlsson, G. Capano, F. A. Lima, J. Rittmann, M. Reinhard, M. H. Rittmann-Frank, O. Braem, E. Baranoff, R. Abela, I. Tavernelli, U. Rothlisberger, C. J. Milne and M. Chergui, *J. Phys. Chem. A*, 2013, **117**, 4591-4601.
195. A. C. Bowman, S. Sproules and K. Wieghardt, *Inorg. Chem.*, 2012, **51**, 3707-3717.
196. R. Sarangi, L. Yang, S. G. Winikoff, L. Gagliardi, C. J. Cramer, W. B. Tolman and E. I. Solomon, *J. Am. Chem. Soc.*, 2011, **133**, 17180-17191.
197. J. Yano, J. Robblee, Y. Pushkar, M. A. Marcus, J. Bendix, J. M. Workman, T. J. Collins, E. I. Solomon, S. DeBeer George and V. K. Yachandra, *J. Am. Chem. Soc.*, 2007, **129**, 12989-13000.
198. E. R. Hall, C. J. Pollock, J. Bendix, T. J. Collins, P. Glatzel and S. DeBeer, *J. Am. Chem. Soc.*, 2014, **136**, 10076-10084.
199. P. J. Riggs-Gelasco, R. Mei, C. F. Yocum and J. E. Penner-Hahn, *J. Am. Chem. Soc.*, 1996, **118**, 2387-2399.
200. C. Goussias, N. Ioannidis and V. Petrouleas, *Biochemistry*, 1997, **36**, 9261-9266.
201. M. Higuchi, T. Noguchi and K. Sonoike, *Biochim. Biophys. Acta Bioenerg.*, 2003, **1604**, 151-158.
202. X. Li, E. M. Sproviero, U. Ryde, V. S. Batista and G. Chen, *Int. J. Quantum Chem.*, 2013, **113**, 474-478.
203. W. M. C. Sameera, C. J. McKenzie and J. E. McGrady, *Dalton Trans.*, 2011, **40**, 3859-3870.
204. K. Yamaguchi, Y. Takahara and T. Fueno, in *Applied Quantum Chemistry*, eds. V. H. Smith Jr., H. F. Scheaffer III and K. Morokuma, D. Reidel, Boston, 1986, pp. 155-184.
205. P. E. M. Siegbahn and R. H. Crabtree, *J. Am. Chem. Soc.*, 1999, **121**, 117-127.
206. P. E. M. Siegbahn, *Chem.—Eur. J.*, 2006, **12**, 9217-9227.
207. I. Zaharieva, M. M. Najafpour, M. Wiechen, M. Haumann, P. Kurz and H. Dau, *Energy Environ. Sci.*, 2011, **4**, 2400-2408.
208. C. Kupitz, S. Basu, I. Grotjohann, R. Fromme, N. A. Zatsepin, K. N. Rendek, M. S. Hunter, R. L. Shoeman, T. A. White, D. Wang, D. James, J.-H. Yang, D. E. Cobb, B. Reeder, R. G. Sierra, H. Liu, A. Barty, A. L. Aquila, D. Deponte, R. A. Kirian, S. Bari, J. J. Bergkamp, K. R. Beyerlein, M. J. Bogan, C. Caleman, T.-C. Chao, C. E. Conrad, K. M. Davis, H. Fleckenstein, L. Galli, S. P. Hau-Riege, S. Kassemeyer, H. Laksmono, M. Liang, L. Lomb, S. Marchesini, A. V. Martin, M. Messerschmidt, D. Milathianaki, K. Nass, A. Ros, S. Roy-Chowdhury, K. Schmidt, M. Seibert, J. Steinbrener, F. Stellato, L. Yan, C. Yoon, T. A. Moore, A. L. Moore, Y. Pushkar, G. J. Williams, S. Boutet, R. B. Doak, U. Weierstall, M. Frank, H. N. Chapman, J. C. H. Spence and P. Fromme, *Nature*, 2014, **513**, 261-265.
209. J. Kern, R. Tran, R. Alonso-Mori, S. Koroidov, N. Echols, J. Hattne, M. Ibrahim, S. Gul, H. Laksmono, R. G. Sierra, R. J. Gildea, G. Han, J. Hellmich, B. Lassalle-Kaiser, R. Chatterjee, A. S. Brewster, C. A. Stan, C. Glöckner, A. Lampe, D. DiFiore, D. Milathianaki, A. R. Fry, M. M. Seibert, J. E. Koglin, E. Gallo, J. Uhlig, D. Sokaras, T.-C. Weng, P. H. Zwart, D. E. Skinner, M. J. Bogan, M. Messerschmidt, P. Glatzel, G. J. Williams, S. Boutet, P. D. Adams, A. Zouni, J. Messinger, N. K. Sauter, U. Bergmann, J. Yano and V. K. Yachandra, *Nat. Commun.*, 2014, **5**, 4371.